

O'NEAL, RYAN, M.S. Molecular Dynamics of $O(^1D) + CCl_4 \rightarrow ClO + CCl_3$ Probed by Cavity-Enhanced Sub-THz Spectroscopy. (2020)
Directed by Dr. Liam M. Duffy. 69 pp.

The UV photodissociation of ozone in the atmosphere is known to result in highly reactive oxygen atoms in their excited $O(^1D)$ electronic state. Subsequent collisions of these atomic radicals with other atmospheric constituents frequently occur without a barrier. Matsumi and Shamsuddin have previously studied the dynamics of these reactions with chlorinated compounds using vacuum-ultraviolet laser-induced fluorescence spectroscopy. In this thesis, we discuss our recent efforts to revisit these experiments by probing the rovibronic distribution of ClO products in hyperfine detail using a recently developed millimeter wavelength cavity enhanced confocal Fabry-Pérot molecular beam spectrometer. In the experiment, ozone is generated and passed over carbon tetrachloride and then the vapor is co-expanded through a pulsed nozzle. The resulting supersonic jet expansion is passed through the beam waste of the Fabry-Pérot while a counter propagating 266 nm photolysis laser initiates the formation $O(^1D)$ atoms and their subsequent intra-beam collision and reaction with CCl_4 . The resulting rovibronic state distribution of the ClO products in this PHOTOLOC-like experiment are then used to confirm whether the reaction occurs via a direct abstraction mechanism, as inferred in the earlier studies. The results have only shown ClO in the ground vibrational state ($v=0$) except for a single signal an excited vibrational state ($v=3$). As it stands, with no other signals being present in the excited vibrational states, we cannot infer the mechanism or molecular dynamics are involved in the reaction to produce ClO from $O(^1D)$ and CCl_4 .

MOLECULAR DYNAMICS OF $O(^1D) + CCl_4 \rightarrow ClO + CCl_3$ PROBED BY CAVITY-
ENHANCED SUB-THz SPECTROSCOPY

by

Ryan O'Neal

A Thesis Submitted to
the Faculty of The Graduate School at
The University of North Carolina at Greensboro
in Partial Fulfillment
of the Requirements for the Degree
Master of Science

Greensboro
2020

Approved by

Committee Chair

APPROVAL PAGE

This thesis, written by Ryan O’Neal, has been approved by the following committee of the Faculty of The Graduate School at The University of North Carolina at Greensboro.

Committee Chair _____

Committee Members _____

Date of Acceptance by Committee

Date of Final Oral Examination

ACKNOWLEDGMENTS

I would like to thank Dr. Liam Duffy for serving as my research advisor throughout these previous years. You have made me a better person since I have joined your lab. I also want to extend a thanks to Dr. Reynaldo Diaz and Michael Shelton for helping me keep the laboratory functioning. As well my committee members Dr. Alice Haddy and Dr. Patricia Reggio.

I want to thank my family, especially my parents, for always being there and supporting me throughout this endeavor.

TABLE OF CONTENTS

| | Page |
|--|------|
| LIST OF TABLES | vi |
| LIST OF FIGURES | vii |
| CHAPTER | |
| I. INTRODUCTION AND OBJECTIVES | 1 |
| II. BACKGROUND | 5 |
| II.A. Reactions of O(¹ D) Atoms with HCl, CCl ₄ , and Chlorofluoromethanes | 5 |
| II.B. Alternative ClO Formation Mechanism Considered | 14 |
| II.C. Subsequent ClO Vibrational Inelastic Scattering | 14 |
| II.D. Introducing the PHOTOLOC Technique | 17 |
| II.E. Limitations of Previous Studies | 21 |
| III. EXPERIMENTAL SETUP | 27 |
| III.A. General Setup for the Experiment | 27 |
| III.B. Ozone Generation and Gas Inlet Manifold | 28 |
| IV. EXPERIMENTAL DATA | 35 |
| IV.A. Nitrous Oxide Signal and Effect of Fabry-Pérot Cavity | 35 |
| IV.B. ClO Product Signal | 38 |
| IV.C. NO Products | 43 |
| V. DISCUSSION OF O(¹ D) + X (CCl ₄ , N ₂ O) REACTIONS | 45 |
| V.A. O(¹ D) + CCl ₄ Reactions | 45 |
| V.B. O(¹ D) + N ₂ O Reactions | 49 |
| V.C. Conclusions | 50 |
| REFERENCES | 52 |
| APPENDIX A. CHLORINE MONOXIDE DATA | 55 |

| | |
|------------------------------------|----|
| APPENDIX B. NITRIC OXIDE DATA..... | 60 |
| APPENDIX C. OTHER DATA | 66 |

LIST OF TABLES

| | Page |
|--|------|
| Table 1. Rotational Temperatures (T_R) for ClO Products Produced from Varying Reactions (Reproduced from Ref. 6) | 8 |
| Table 2. Franck-Codon Factors Produced for ClO from the RKR Potential Calculations (Reproduced from Ref. 6) | 9 |
| Table 3. Summary Table of Chlorine Monoxide Data in Appendix A..... | 55 |
| Table 4. Summary Table of Nitric Oxide Data in Appendix B | 60 |

LIST OF FIGURES

| | Page |
|---|------|
| Figure 1. ClO Product Emission Spectrum from $C^2\Sigma^- v = 0 - X^2\Pi v = 1$ from the Reaction $O(^1D) + CF_2Cl_2$ (Reproduced from Ref. 6)..... | 7 |
| Figure 2. Boltzmann Plot for ClO Rotational Distribution (Reproduced from Ref. 6)..... | 8 |
| Figure 3. Relative Populations of ClO Product Vibrational Levels (Reproduced from Ref. 6) | 10 |
| Figure 4. Energy Diagram for the Different Isomeric Forms of HOCl (Reproduced from Ref. 6) | 12 |
| Figure 5. Rotational Distributions of O ₂ and ClO Overlapping Each Other (Reproduced from Ref. 10) | 15 |
| Figure 6. Vibrational Distribution of ClO (Reproduced from Ref. 10) | 16 |
| Figure 7. Vibrational Distribution of O ₂ (Reproduced from Ref. 10) | 16 |
| Figure 8. Collapsed Newtonian Diagram for PHOTOLOC (Redrawn from Ref. 3)..... | 19 |
| Figure 9. A Semiconfocal Cavity Moving Through a Beam Splitter (Redrawn from Ref. 4)..... | 24 |
| Figure 10. Semiconfocal Cavity But the Photons Move to an Off-Axis Detector (Redrawn from Ref. 4) | 24 |
| Figure 11. Cutaway View of Duffy Lab Mm/Submillimeter-Wave Molecular Beam Setup with Conventional Pass-Through Confocal Fabry-Pérot Resonator..... | 27 |
| Figure 12. O ₃ Absorption Signal with a Hole Generated by the 266 nm Output of a Nd:YAG Laser | 31 |
| Figure 13. Simplified Gas Inlet Manifold | 32 |
| Figure 14. Carbon Tetrachloride Setup | 33 |

| | |
|---|----|
| Figure 15. Absorption (V) of N ₂ O with the Z-Axis is the Absorption Signal (Volts), Y-Axis Shows Frequency (MHz), and Time (μsecs) on the X-Axis at a Center Frequency of 100491.740000 MHz | 35 |
| Figure 16. Absorption and Dispersion Signal of N ₂ O in the Presence of the Fabry-Pérot Cavity Tuned to be Coincident With the Line Center Frequency of 100491.740000 MHz | 36 |
| Figure 17. Absorption Signal for ClO Product Molecules in the Ground Vibrational State | 40 |
| Figure 18. Absorption Signal for ClO While Using a Slit Nozzle With a Center Frequency of 167195.838000 MHz, Transitions Were N = 4 ← 3, Λ = -1 ← 1, ν = 0 ← 0, J = 4.5 ← 3.5, F = 6 ← 5 | 41 |
| Figure 19. Signal for ClO While Using a Pinhole Nozzle With a Center Frequency of 167195.838000 MHz, Transitions Were N = 4 ← 3, Λ = -1 ← 1, ν = 0 ← 0, J = 4.5 ← 3.5, F = 6 ← 5 | 42 |
| Figure 20. Absorption Signal for a Vibrationally Excited ClO Product Signal With a Center Frequency of 198468.5256 MHz, Transitions Were N = 5 ← 4, Λ = -1 ← 1, ν = 3 ← 3, J = 5.5 ← 4.5, F = 6 ← 5 | 42 |
| Figure 21. Absorption Signal for NO With a Center Frequency of 150546.520000 MHz, Transitions Were N = 2 ← 1, Λ = 1 ← -1, ν = 0 ← 0, J = 1.5 ← 0.5, F = 2.5 ← 1.5 | 43 |
| Figure 22. Absorption Signal for NO With a Center Frequency of 250436.848000 MHz, Transitions Were N = 3 ← 2, Λ = 1 ← -1, ν = 0 ← 0, J = 1.5 ← 0.5, F = 3.5 ← 2.5 | 44 |
| Figure 23. The Top Picture Shows the Frequencies for ClO That are Accessible Within Our Frequency Sources With the Middle Picture Showing One Rotational State Shown in Hyperfine Detail | 55 |
| Figure 24. Absorption Signal for ClO With a Center Frequency of 167137.754900 MHz, Transitions Were N = 4 ← 3, ν = 0 ← 0, J = 4.5 ← 3.5, F = 5 ← 5 | 56 |
| Figure 25. Absorption Signal for ClO With a Center Frequency of 167175.070600 MHz, Transitions Were N = 4 ← 3, Λ = 1 ← -1, ν = 0 ← 0, J = 4.5 ← 3.5, F = 4 ← 4 | 56 |

| | |
|--|----|
| Figure 26. Absorption Signal for ClO With a Center Frequency of 167195.838000 MHz, Transitions Were $N = 4 \leftarrow 3$, $\Lambda = -1 \leftarrow 1$, $v = 0 \leftarrow 0$, $J = 4.5 \leftarrow 3.5$, $F = 6 \leftarrow 5$ | 57 |
| Figure 27. Absorption Signal for ClO With a Center Frequency of 167201.760800 MHz, Transitions Were $N = 4 \leftarrow 3$, $\Lambda = 1 \leftarrow -1$, $v = 0 \leftarrow 0$, $J = 4.5 \leftarrow 3.5$, $F = 3 \leftarrow 3$ | 57 |
| Figure 28. Absorption Signal for ClO With a Center Frequency of 204345.751100 MHz, Transitions Were $N = 5 \leftarrow 4$, $\Lambda = -1 \leftarrow 1$, $v = 0 \leftarrow 0$, $J = 5.5 \leftarrow 4.5$, $F = 7 \leftarrow 6$ | 58 |
| Figure 29. Absorption Signal for ClO With a Center Frequency of 241489.781700 MHz, Transitions Were $N = 6 \leftarrow 5$, $v = 0 \leftarrow 0$, $J = 6.5 \leftarrow 5.5$, $F = 8 \leftarrow 7$ | 58 |
| Figure 30. Absorption Signal for ClO With a Center Frequency of 278627.100200 MHz, Transitions Were $N = 7 \leftarrow 6$, $N = 0 \leftarrow 0$, $J = 7.5 \leftarrow 6.5$, $F = 9 \leftarrow 8$ | 59 |
| Figure 31. 2-D of Figure 20, Absorption Signal for ClO With a Center Frequency of 198468.525600 MHz, Transitions Were $N = 5 \leftarrow 4$, $\Lambda = -1 \leftarrow 1$, $v = 3 \leftarrow 3$, $J = 5.5 \leftarrow 4.5$, $F = 7 \leftarrow 6$ | 59 |
| Figure 32. Frequencies for NO That are Accessible Within our Frequency Domain with One Rotational State Show in Detail to Show Multiple Line Frequencies and Their Transitions..... | 60 |
| Figure 33. Absorption Signal for NO With a Center Frequency of 150176.480000 MHz, Transitions Were $N = 2 \leftarrow 1$, $\Lambda = -1 \leftarrow 1$, $v = 0 \leftarrow 0$, $J = 1.5 \leftarrow 0.5$, $F = 2.5 \leftarrow 1.5$ | 61 |
| Figure 34. Absorption Signal for NO With a Center Frequency of 150225.660000 MHz, Transitions Were $N = 2 \leftarrow 1$, $\Lambda = -1 \leftarrow 1$, $v = 0 \leftarrow 0$, $J = 1.5 \leftarrow 0.5$, $F = 0.5 \leftarrow 0.5$ | 61 |
| Figure 35. Absorption Signal for NO With a Center Frequency of 150546.520000 MHz, Transitions Were $N = 2 \leftarrow 1$, $\Lambda = 1 \leftarrow -1$, $v = 0 \leftarrow 0$, $J = 1.5 \leftarrow 0.5$, $F = 2.5 \leftarrow 1.5$ | 62 |
| Figure 36. Absorption Signal for NO With a Center Frequency of 150580.560000MHz, Transitions Were $N = 2 \leftarrow 1$, $\Lambda = 1 \leftarrow -1$, $v = 0 \leftarrow 0$, $J = 1.5 \leftarrow 0.5$, $F = 0.5 \leftarrow 0.5$ | 62 |

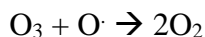
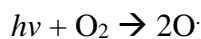
| | |
|---|----|
| Figure 37. Absorption Signal for NO With a Center Frequency of 250436.8480 MHz, Transitions Were $N = 3 \leftarrow 2$, $\Lambda = 1 \leftarrow -1$, $v = 0 \leftarrow 0$, $J = 2.5 \leftarrow 1.5$, $F = 3.5 \leftarrow 2.5$ | 63 |
| Figure 38. Absorption Signal for NO With a Center Frequency of 250440.6590 MHz, Transitions Were $N = 3 \leftarrow 2$, $\Lambda = 1 \leftarrow -1$, $v = 0 \leftarrow 0$, $J = 2.5 \leftarrow 1.5$, $F = 2.5 \leftarrow 1.5$ | 63 |
| Figure 39. Absorption Signal for NO With a Center Frequency of 250448.530000 MHz, Transitions Were $N = 3 \leftarrow 2$, $\Lambda = 1 \leftarrow -1$, $v = 0 \leftarrow 0$, $J = 2.5 \leftarrow 1.5$, $F = 1.5 \leftarrow 0.5$ | 64 |
| Figure 40. Absorption Signal for NO With a Center Frequency of 250475.414000 MHz, Transitions Were $N = 3 \leftarrow 2$, $\Lambda = 1 \leftarrow -1$, $v = 0 \leftarrow 0$, $J = 2.5 \leftarrow 1.5$, $F = 1.5 \leftarrow 1.5$ | 64 |
| Figure 41. Absorption Signal for NO With a Center Frequency of 250482.939000 MHz, Transitions Were $N = 3 \leftarrow 2$, $\Lambda = 1 \leftarrow -1$, $v = 0 \leftarrow 0$, $J = 2.5 \leftarrow 1.5$, $F = 2.5 \leftarrow 2.5$ | 65 |
| Figure 42. Scan of the Fabry-Pérot Cavity Resonance | 66 |
| Figure 43. Absorption Signal for Magnetic Dipole Allowed Transition of O ₂ With a Center Frequency of 62486.259400 MHz, Transitions Were $N = 3 \leftarrow 3$, $J = 0 \leftarrow 0$, $F_1 = 0 \leftarrow 0$, $F_2 = 3 \leftarrow 2$ | 66 |
| Figure 44. Absorption Signal for O ₂ With a Center Frequency of 62486.259400 MHz, Transitions Were $N = 3 \leftarrow 3$, $J = 0 \leftarrow 0$, $F_1 = 0 \leftarrow 0$, $F_2 = 3 \leftarrow 2$ | 67 |
| Figure 45. Absorption Signal for O ₂ With a Center Frequency of 62486.259400 MHz, Transitions Were $N = 3 \leftarrow 3$, $J = 0 \leftarrow 0$, $F_1 = 0 \leftarrow 0$, $F_2 = 3 \leftarrow 2$ | 67 |
| Figure 46. Absorption Signal for O ₂ With a Center Frequency of 62486.259400 MHz, Transitions Were $N = 3 \leftarrow 3$, $J = 0 \leftarrow 0$, $F_1 = 0 \leftarrow 0$, $F_2 = 3 \leftarrow 2$ | 68 |
| Figure 47. Absorption Signal for O ₂ With a Center Frequency of 62486.259400 MHz, Transitions Were $N = 3 \leftarrow 3$, $J = 0 \leftarrow 0$, $F_1 = 0 \leftarrow 0$, $F_2 = 3 \leftarrow 2$ | 68 |

Figure 48. Absorption Signal for O₂ With a Center Frequency of 62486.259400 MHz, Transitions Were N = 3 ← 3, J = 0 ← 0, F₁ = 0 ← 0, F₂ = 3 ← 2.....69

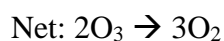
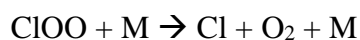
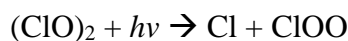
CHAPTER I

INTRODUCTION AND OBJECTIVES

Ozone (O₃), which exists throughout the atmosphere, is continually forming and degrading away in a naturally occurring cycle which can be seen below.



Although it is an inhalation health hazard at ground level, stratospheric ozone is known to prevent harmful UV radiation from reaching Earth's surface. In the late 1970s, data supported the idea that the ozone layer found in polar regions of the stratosphere, particularly over Antarctica, was being destroyed by processes that were not natural. Ozone depletion can occur when hydroxyl radicals, nitric oxide radicals, or bromine/chlorine radicals disrupt the normal cycle between O₂ and O₃. Over the years, the depletion was becoming larger and larger, and the concern was that human activity might be the root cause. This was, in fact, the case, and a destructive catalytic cycle was discovered and published by the 1995 Noble laureates Mario Molina, and Frank Rowland. Their work showed that man-made chlorofluorocarbons (CFCs) were damaging to the ozone layer and that they were the cause of 75 % of the damage done to the ozone with the pathway shown below.



Once the cause was discovered to be man-made, international policymakers got together in Montreal, Canada and put together what is known as the Montreal Protocol to assess which chemicals were ozone-destroying and to phase them out over time.¹² The protocol went into effect in 1989, and the ozone levels slowly started recovering with inorganic chlorine concentrations declining at a rate of about 0.8%/year.² As a result, the Montreal Protocol is often cited as one of the most effective measures taken by humanity to fight man-made environmental issues, and as such, has often been held up as evidence that the international community can come together to find solutions to problems on a global scale such as global warming.

Beyond the catalytic cycle written above, scientists have teased out the kinetics of many chemical reaction pathways that impact the concentration of atomic chlorine and ClO radicals and hence ozone concentrations in the atmosphere. Kineticists have carefully studied so-called chlorine "reservoir molecules" like ClO, ClO₂ and chlorofluorocarbons and their atmospheric reactions and photochemistry over the years to measure and model the ozone loss rates, concentrations, and ultimately to inform policy decisions going forward.

While the kinetics and energetics of reservoir molecule chemistry have been studied, the detailed physics of these reactions and related photochemistry have similarly been studied by scientists in the Chemical Physics / Physical Chemistry community, to understand the detailed quantum mechanical reaction mechanisms. This field is known as Molecular Reaction Dynamics. While this work is fundamental, scientists must know the mechanisms at work that cause physical or chemical changes in reactions.

One method for experimentally studying molecular reaction dynamics is in crossed molecular beams (CMB), where two skimmed and columnated molecular beams of reactant species intersect in a vacuum chamber. The resulting products are then probed by a variety of techniques such as Time of Flight Mass Spectrometry (ToF-MS) or Laser-Induced Fluorescence (LIF). Similarly, reactants may be introduced and flow through a gas cell; these are often referred to as “bulb” experiments. This latter, bulb method, was performed by researchers Matsumi and Shamsuddin which used the fluorescence of laser-excited ClO product molecules to determine their nascent vibrational and rotational state populations following the reactions of O(¹D) atoms reacting with HCl, CCl₄ and Chlorofluoromethanes.⁶

A similar experimental method initiates the reaction in a molecular beam rather than a simple gas cell. By crossing a laser with the molecular beam, the reactants start out colder and thereby occupy fewer initial rotational and vibrational states prior to reaction. In these experiments, the electric vector of the laser then also defines an axis for probing the angular distribution of the products. This method, which was first introduced by Zare and coworkers, is referred to as PHOTOLOC (photoinitiated reaction analyzed by the law

of cosines).³ In our experiments, we will use a method like PHOTOLOC, where only one molecular beam is used instead of a crossed molecular beam.³ It permits measurements of the center-of-mass angular distributions across the entire scattering angular range unlike CMB's where there would be a limit to the angular range dependent on the beams and the orientation of the beams for the collisions to occur.

The primary objectives of my research are to combine the mm-wavelength direct absorption molecular beam technique developed in the Duffy group with the PHOTOLOC method, to: (1) measure the translational, rotational, vibrational, electronic and hyperfine energy distributions of ClO products following the reaction of O(¹D) + CCl₄ and (2) to use these results to infer the molecular dynamics behind the O(¹D) radical attack on carbon tetrachloride to form ClO. This experiment will be made possible by the Duffy group's recently developed mm-wave Fabry-Pérot resonance cavity to enhance the signal sensitivity of the setup. The next section will discuss the historical studies of CCl₄ and other chlorofluorocarbons reactions that produce ClO followed by a study on Fabry-Pérot cavities with the following sections discussing the experimental procedures and setup, preliminary data, and future work, respectively.

CHAPTER II

BACKGROUND

Stratospheric ozone protects life by absorbing harmful high energy UV radiation through the photodissociative reaction: $O_3 + h\nu \rightarrow O(^1D \text{ or } ^3P) + O_2$. At wavelengths ranging from 230-296 nm (297 ± 2 K), the electronically excited $O(^1D)$ atoms are preferentially produced over ground state $O(^3P)$ atoms with a quantum yield ranging from 0.881-0.928 (1.00 being 100 % yield).¹¹ These excited $O(^1D)$ atoms are in turn extremely reactive, and may then go on to react with chlorofluorocarbons, producing ClO and thereby directly accelerating the destructive catalytic ozone cycle outline above. Concentrations of ClO in the stratosphere have been measured and modeled by kineticists and are found to correlate with ozone concentrations inversely.⁶ The Molecular Reaction Dynamics community has attempted to understand the quantum mechanical mechanism of these atmospherically important reactions by measuring the quantum state distribution of the ClO products. The reactions are highly exoergic; the ensuing dynamics result in ClO products with vibrationally inverted, non-Boltzmann, quantum state distributions, as described below.

II.A. Reactions of $O(^1D)$ Atoms with HCl, CCl_4 , and Chlorofluoromethanes

Researchers Matsumi and Shamsuddin attempted to find the nascent vibrational, rotational and electronic state-energy distributions of ClO by dissociating ozone to produce $O(^1D)$ and have it reacted with HCl, CCl_4 , and other chlorofluoromethanes.

Ozone was mixed at 20 mTorr with 80 mTorr of the chlorinated species under continuous flow conditions using a gas reaction flow cell at room temperature. The 248 nm output of a KrF excimer laser then caused the photolysis of ozone and the subsequent production of the reactive O(¹D) atoms. For this type of experiment where products need to be in their nascent state following reaction, a lower number of collisions between particles are preferred. It is worth pointing out here that a key advantage of the molecular beam based experiments outlined in this thesis is that the collision rate is greatly reduced due to the much lower translational temperature (1-10 K) of the gas within the beam. This dramatic cooling is an effect of the isentropic expansion which also maintains a relatively high number density along the molecular beam axis. Collision rates within a molecular beam can be even further reduced, assuming the same density of particles at the same temperature, molecular beams have a directional component which reduces the collision rate by as much as a factor of three when compared to a reaction cell,

To determine if ClO radicals were produced, they used a vacuum ultraviolet laser-induced fluorescence (VUV LIF) technique which excited ClO radicals to an excited energy level ($C^2\Sigma^- - X^2\Pi_{3/2}$). The VUV was generated by four-wave mixing with Xe gas using two dye lasers pumped by a XeCl excimer laser⁶. ClO will eventually fluoresce back to its ground state and in doing so will emit a photon, but at a longer wavelength which can be detected, for this, the researchers monitored the reaction cell using a VUV monochromator and a solar-blind photomultiplier.⁶ Their spectrum for ClO from the reaction of O(¹D) + CF₂Cl₂ can be seen in Figure 4 with the top being the experimental data and the lower panel being data from a simulation and the two matching closely.

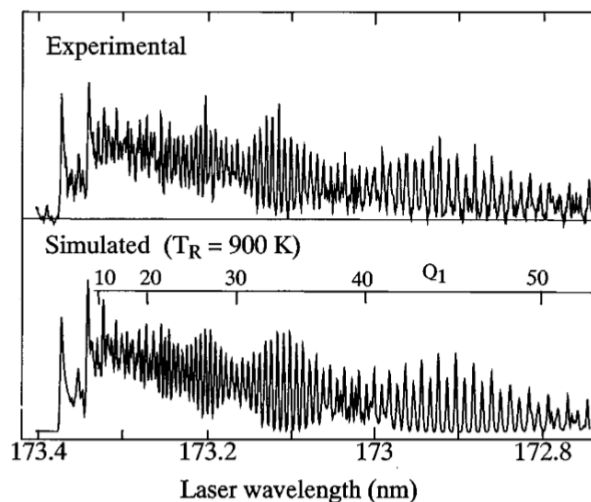


Figure 1. CIO Product Emission Spectrum from $C^2\Sigma^- v = 0 - X^2\Pi v = 1$ from the Reaction $O(^1D) + CF_2Cl_2$ (Reproduced from Ref. 6).

Figure 1 shows the fluorescence peaks for the Q branch for varying rotational states. The researchers were able to obtain the rotational temperatures of CIO from the reactions of $O(^1D)$ with HCl, CCl_4 , $CFCl_3$, and CF_3Cl , which can be seen for reference in table 1. Knowing the rotational temperatures, they give an example of CIO rotational distribution from the reaction $O(^1D) + HCl$ shown in Figure 2 with the temperature of the reaction (2050 ± 60 K) in Table 1. Interestingly though, they did not obtain a rotational distribution for the reaction of CCl_4 because they discovered an unknown fluorescence emission from CCl_4 which interfered with the CIO product fluorescence they were trying to detect.⁶

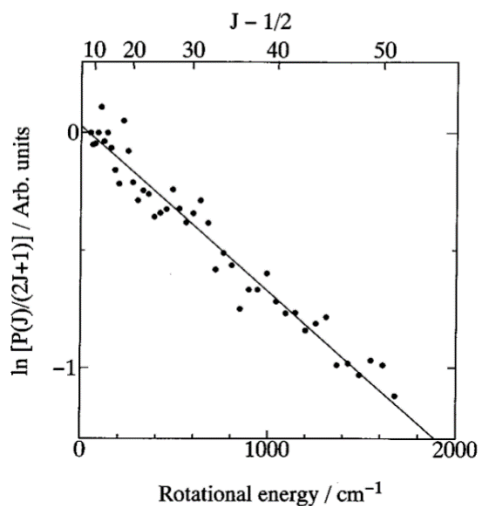


Figure 2. Boltzmann Plot for ClO Rotational Distribution (Reproduced from Ref. 6).

Table 1. Rotational Temperatures (T_R) for ClO Products Produced from Varying Reactions (Reproduced from Ref. 6)

| Reactant | ClO(ν) | T_R |
|---------------------------------|--------------|----------------|
| HCl | 0 | 2050 ± 60 |
| | 1 | 1770 ± 180 |
| CF ₃ Cl | 0 | 900 ± 100 |
| | 1 | 900 ± 100 |
| CF ₂ Cl ₂ | 0 | 900 ± 100 |
| | 1 | 900 ± 100 |
| CFCl ₃ | 0 | 1000 ± 100 |

Argon was added to the Matsumi and Shamsuddin experiments to relax the rotational distributions by having the Argon collide with, but not react with, ClO. It takes fewer collisions to thermalize a rotational distribution in contrast to a vibrational distribution where geometric constraints require smaller impact parameters and end-on collisions to convert ClO vibrational energy to translational and/or rotational energy and hence relax ClO vibrationally. Matsumi and Shamsuddin were able to confirm this by

changing the delay in time between 2 and 10 μs and finding the vibration distribution had not changed. Before transition intensities could be correlated to product state populations, the line intensities had to first be normalized with respect to laser power and transition Frank-Condon (FC) factors. This is because some transition wave functions overlap better than others; higher FC values mean better overlap of wave functions and higher inherent luminosity even for equivalent state populations. Matsumi and Shamsuddin determined the appropriate FC factors seen in table 2 by using the Rydberg-Klein-Rees (RKR) potentials. Signal intensities were then normalized by dividing the line intensities by their FC values and VUV laser power output.

Table 2. Franck-Condon Factors Produced for ClO from the RKR Potential Calculations (Reproduced from Ref. 6)

| v''/v' | 0 | 1 | 2 | 3 |
|----------|--------|--------|--------|--------|
| 0 | 0.3093 | 0.3834 | 0.2156 | 0.0760 |
| 1 | 0.3379 | 0.0097 | 0.1473 | 0.2714 |
| 2 | 0.2067 | 0.0947 | 0.1357 | 0.0074 |
| 3 | 0.0939 | 0.1952 | 0.0000 | 0.1563 |
| 4 | 0.0354 | 0.1620 | 0.0831 | 0.0465 |
| 5 | 0.0118 | 0.0908 | 0.1503 | 0.0084 |
| 6 | 0.0036 | 0.0406 | 0.1286 | 0.0869 |

Once normalized, the relative line intensities gave the ClO vibrational distributions seen in Figure 3, below.

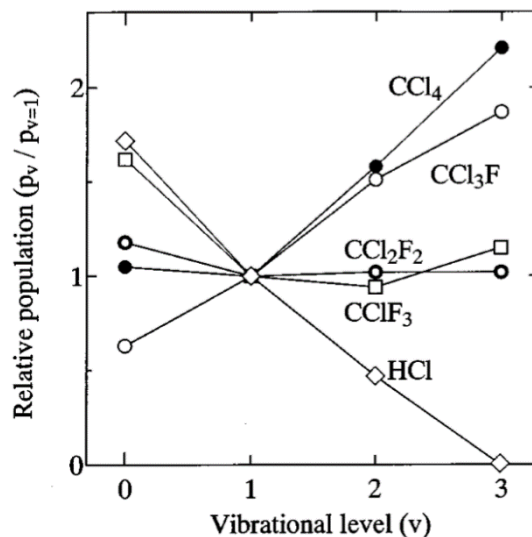


Figure 3. Relative Populations of ClO Product Vibrational Levels (Reproduced from Ref. 6).

Figure 3 presents all five reactants involved with them normalized to the $v=1$ population of ClO and shows that for CCl₄ and CCl₃F, the ClO populations seemed to increase with increasing vibration states while HCl was the inverse.

Matsumi and Shamsuddin showed that the Franck-Condon factors were small for vibronic bands $v \geq 4$ for $X^2\Pi$ to $C^2\Sigma^-$ and they have made the argument, outlined below, that any transitions to a vibrational level higher than $v' = 0$ in $C^2\Sigma^-$ would be predissociative; vibrational levels up to $v = 18$ in the $X^2\Pi$ state are energetically possible for CCl₄. Using LIF, they normalized the band intensity to $(v', v'' = 1, 0)$ with the probe laser power but soon discovered the $(1, 0)$ band intensity is ten times weaker than the $(0, 0)$ band intensity. This is surprising given that the Franck-Condon factors calculated for the transitions were similar, indicating that the intensities should have been similar. Matsumi and Shamsuddin proceeded to probe the $(2, 0)$, $(2, 1)$, and $(2, 2)$ bands but concluded no

signals were found. The researchers did observe the (3,3) band. Having the band intensities decline once bands $v' \geq 1$ range for $C^2\Sigma$ very well could indicate predissociation is occurring and it is happening faster than radiative emission which explains the lack of signals in bands (2, $v'' = 0-2$). The notable exception being the intensity detected for the (3,3) band. Matsumi and Shamsuddin argue that the rate of predissociation might be slightly slower for the 3rd vibrational level compared to the 1st and 2nd.⁷ To determine if the rotational dependent predissociation occurs, the researchers allowed for a long-time delay of 40 μ s so the ClO $X^2\Pi$ rotational distribution could be allowed to relax to room temperature (300 K). Once at room temperature, they compared the simulated spectrum to the experimentally obtained spectrum and found it was similar. This indicated that the $^2\Sigma^- - ^2\Pi$ transition showed no signs of J-dependent predissociation in the $C^2\Sigma v' = 0$ spectrum range.

Focusing on the reaction of $O(^1D) + HCl$, Matsumi and Shamsuddin used an energy diagram created by SCF-CI calculations performed by Bruna et al. to help determine which channel would be most likely. Figure 4 below shows the energy diagram for $O(^1D) + HCl$, which shows the two isomeric forms of the intermediates with their own energies.⁶

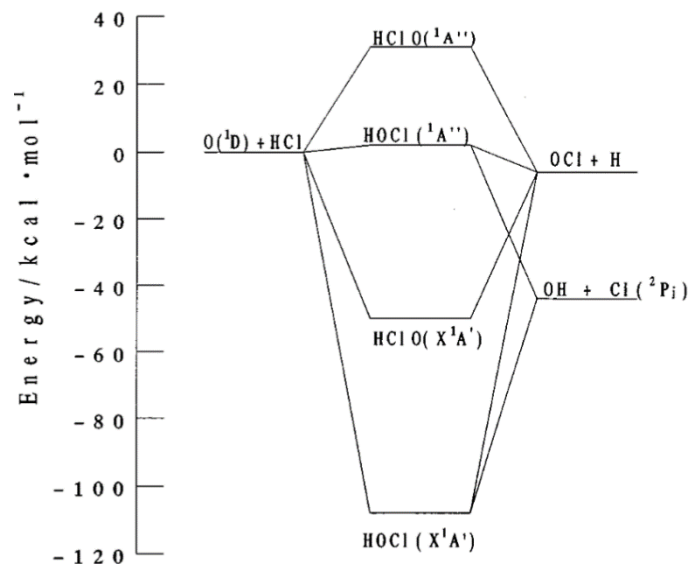


Figure 4. Energy Diagram for the Different Isomeric Forms of HOCl (Reproduced from Ref. 6).

HOCl (X^1A') can be observed having a well of about $-110 \text{ kcal mol}^{-1}$ with respect to the starting reactants. The possible products of this pathway are OH + Cl(1P_j) and ClO + H, and of the two, OH + Cl(1P_j) has the most significant likelihood of being the final products because of the energy difference between the two products it requires $38.1 \text{ kcal mol}^{-1}$ less energy than ClO + H.⁶ The isomeric form of HClO (X^1A') requires more energy than HOCl (X^1A') which makes it less likely, but it only has one product channel which is ClO + H. Matsumi et al. did work previously on the branching ratio between the two products finding the ratio to be 0.24 ± 0.06 ($[\text{OCl} + \text{H}]/([\text{OH} + \text{Cl}]$).⁸ They performed the same experiment with deuterium and found the branching ratio with H to be three times larger than with deuterium.

The two possible reaction mechanisms to create the ClO or OH products are an *insertion* of the O(1D) followed by decomposition or a direct *abstraction* of the chlorine

atom or proton. They suggest that the velocity of the H atom, being twice that of the deuterium, might explain the significant difference between the two isotopes and help determine the mechanism that is occurring. The H atom moves much faster than the O or Cl atoms, so when the O(¹D) gets close to the HCl, the H atom is removed from the Cl atom and is far from it so by the time the O(¹D) gets to the Cl atom the potential surface will become covalent.⁸ With half the velocity, the deuterium has less time to escape and allow this abstraction method to happen less frequently. Another pathway is possible though, instead of a direct “attack” on the HCl, it might also come at a sidewise angle to form the other isomeric intermediate HOCl and then decompose into OH + Cl products. A change in the approach of symmetry for ¹A'' could also lead to the ClO +H pathway. Researchers Kruus et al. detected HCl molecules that were excited vibrationally which they argued could result from an electronic-vibrational (E-V) energy transfer and that the O(¹D) transfers electronic energy to vibrational energy for HCl and transforms into O(³P).⁸

Reaction pathways involving O(¹D) + chlorofluoromethanes are like HCl with abstraction and insertion/decomposition being the possible mechanisms involved. The insertion mechanism argues that for O(¹D) + chlorofluoromethanes or CCl₄, O(¹D) gets between the C and Cl atoms and forms a vibrationally excited hypochlorite (COCl) and then soon decomposes into the product ClO.⁶ The abstraction mechanism can also be argued for in these reactions where the ClO bond is formed early in the approach of O(¹D) atom. This “early” transition state geometry looks more like the reactant geometry O---Cl-CX than the product geometry O-Cl---CX. Once past the early transition state, the

quasi-free Cl atom accelerates towards the O(¹D) atom. This then forms a ClO bond that is vibrationally excited and hence leads to an “inverted” ClO vibrational population distribution.

II.B. Alternative ClO Formation Mechanism Considered

A different research team, Addison et al., also experimented with the reaction of O(¹D) + CF₃Cl to try and discover which mechanism produced ClO. Matsumi and Shamsuddin and Addison et al. considered insertion or abstraction mechanisms, but Addison et al. also proposed an additional third “displacement” mechanism another was direct abstraction of the Cl atom to form products of ClO and CF₃, and then displacement of the Cl atom with O(¹D)).^{6,9} The displacement mechanism allows the formation of CF₃O + Cl with the Cl atom then reacting with ozone to form ClO + O₂. To test this, the researchers added ethane to the mixture of O₃ and CF₃Cl; the idea is that any chlorine radicals produced from the displacement mechanism will not be able to react with ozone because of the free chlorine atoms will react with ethane. A noticeable reduction of ClO should be seen if displacement was, in fact, the mechanism at work, but the results only showed a minor reduction of ClO products. This suggests that chlorine atoms were not liberated in the reaction, and hence the ClO products observed were only from an insertion or abstraction mechanism.

II.C. Subsequent ClO Vibrational Inelastic Scattering

Researchers Teixeira and Varandas studied what happens between ClO and O₂ and if their collisions would or could change their nascent vibrational states. Figure 5

below shows where they overlaid the rotational distributions of ClO and O₂ from the reaction of Cl + O₃ with the focus being that they only slightly overlay each other.¹⁰

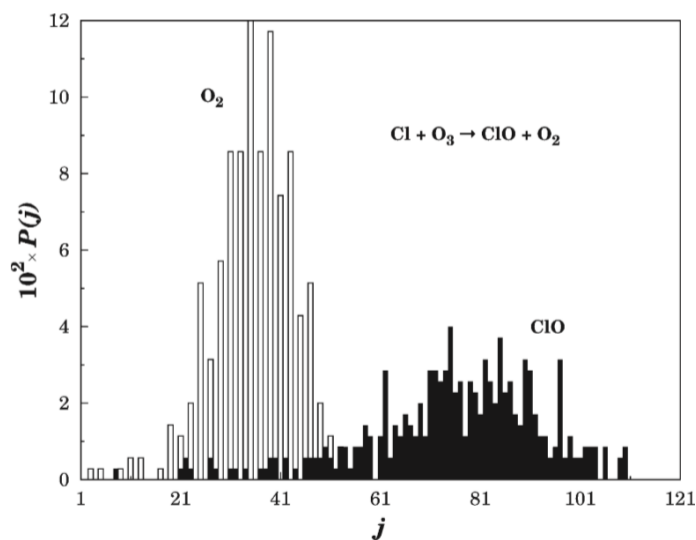


Figure 5. Rotational Distributions of O₂ and ClO Overlapping Each Other (Reproduced from Ref. 10).

Since the distributions follow a Boltzmann distribution, we can see that at 300 K the distributions between the two are different because of the difference in their rotational constant. The figure shows that it is not likely that a single temperature can be attributed to both compound distributions.¹⁰ Teixeira and Varandas then move onto investigating the inelastic collision process that takes place between ClO and O₂ with Figures 6 and 7 showing the vibrational distributions of ClO and O₂ respectively.

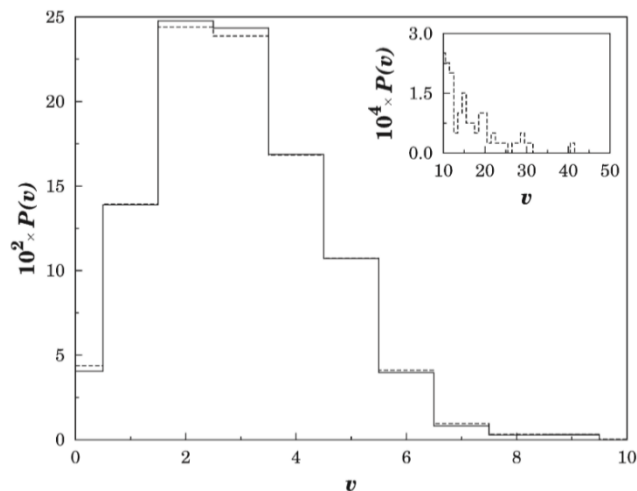


Figure 6. Vibrational Distribution of ClO (Reproduced from Ref. 10).

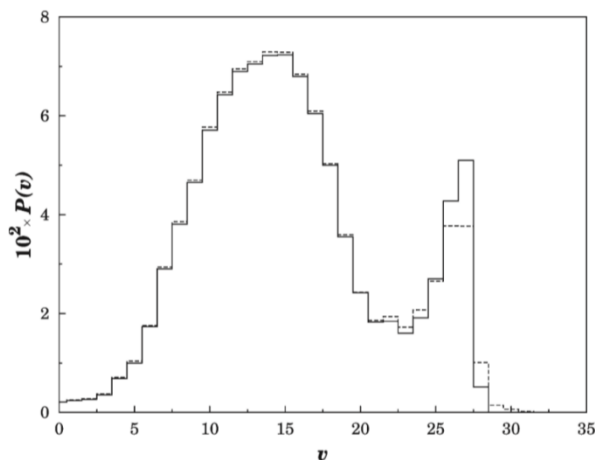


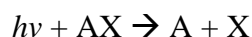
Figure 7. Vibrational Distribution of O₂ (Reproduced from Ref. 10).

For ClO, the vibrational distributions show the most particles populated at $v = 2$ with $v = 3$ being close in population with vibrational levels being populated to $v = 9$ with the temperature of the inelastic collision process was at 250 K.¹⁰ Figure 7 shows that the vibrational distribution for O₂ is most populated at $v = 15$ with the highest vibrational state being $v = 31$. Teixeira and Varandas ran trajectory calculations and discovered that

there is no real difference between the steady-state distributions and nascent distributions and that a collision between vibrationally excited O₂ and ClO might not form O₃ on their first collisions but still do so in later collisions.

II.D. Introducing the PHOTOLOC Technique

In 1999 researchers Fernandez-Alonso, Bean, and Zare introduced the PHOTOLOC technique which can be used when the reactions involved can be represented as:



where X is photodissociated from A, and the A fragments then go on to collide with the BC molecule to generate AB and C products.³ If AX and BC are co-expanded into a vacuum together to form a supersonic-jet molecular beam, then AX and BC will have nearly zero relative speed to one another. In this case then the relative velocity of the reactants is determined by the bond dissociation energy the photolytic precursor (AX) and the photolysis wavelength.³ This is the first element of PHOTOLOC, i.e., the photolysis of a photolytic precursor. It is possible to find the translational energy of photofragment A from the equation below:

$$E_A = \left(\frac{m_A}{m_{AX}} \right) * (h\nu - \Delta E_{AX}), \quad (1)$$

where m_A and m_{AX} are the masses of fragment A, and molecule AX, respectively, ΔE_{AX} is the endoergicity required for bond dissociation, and $h\nu$ is the photolysis laser photon

energy.³ Since AX and BC have zero relative velocity, they appear to be stationary to one another before photolysis. Following photolysis, atom A travels towards molecule BC. The center-of-mass (COM) of the A + BC system lies along the axis between the atom and the molecule. The center-of-mass moves through the laboratory frame of reference with a velocity u_{CM} and linear momentum Mu_{CM} which must be conserved before, during, and even following the reaction; M is the sum of masses m_A and m_{BC} . This COM velocity can be determined by using the equation:

$$u_{CM} = \left(\frac{m_A}{M}\right) * \sqrt{\frac{2*E_A}{m_A}} \quad (2)$$

If dealing with a specific AB molecule with a specific vibrational and rotational state which has a known endoergicity, we can find that the magnitude of the center-of-mass speed to be the equation:

$$u_{AB} = \left(\frac{m_c}{M}\right) * \sqrt{\frac{2*\left(\frac{\mu}{m_A}\right)*E_A - \Delta E}{\mu'}} \quad (3)$$

With μ and μ' being the reduced masses of the reagent and product collision partners, respectively.³ Reduced mass takes a two-body problem (in this case AB) and reduces it a one-body problem by finding the “effective” inertial mass between the two bodies with the equation being presented below as equation 6:

$$\mu = \frac{m_A m_B}{m_A + m_B}, \quad (4)$$

where m_A is the mass of atom A and m_B being the mass of atom B. Taking these equations leads to the second element of the two elements of PHOTOLOC, which is the law of cosines and how to relate the product laboratory velocity distribution to the center-of-mass product angular distribution with the law of cosines which can be seen in equation 7:³

$$v_{AB}^2 = u_{CM}^2 + u_{AB}^2 + 2u_{CM}u_{AB}\cos(\theta) \quad (5)$$

When combined, the velocities can act as the sides of a triangle represented as a collapsed Newton diagram which can be seen below in Figure 8.

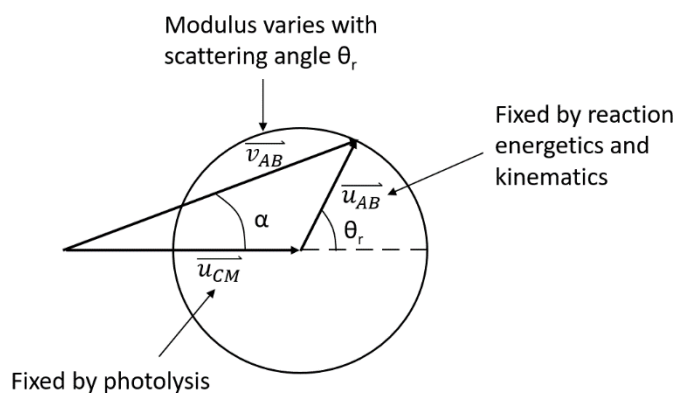


Figure 8. Collapsed Newtonian Diagram for PHOTOLOC (Redrawn from Ref. 3).

This helps establish a relationship between the angular product distribution measured in the laboratory frame of reference and the same angular distribution in the center-of-mass frame of reference, i.e., the colliding molecule's frame of reference. Instead of a cross molecular beam set up, PHOTOLOC allows for a simpler single molecular beam approach. Not only is the relative collision energy fixed by the

photolysis process, but the subsequent $AB + C$ reaction products may also display a memory of the collision geometry. For example, if the ABC collision complex (transition state) exists for less time than a rotational period, then the ensuing products may emerge more on one side of the Newton sphere in Figure 8 above, than on the other. Conversely, if the complex lives for some considerable time, the tumbling of the complex will wash out any memory of the original collision geometry and the products will appear uniformly, i.e., isotropically, over the sphere. In our case, insertion vs. abstract mechanisms should lead to isotropic and anisotropic angular product distributions, respectively. Hence, angular product scattering information can convey information about the underlying reaction dynamics.

Different experimental methods exist for determining product scattering angular distributions in the laboratory frame of reference. If spectroscopic methods are used, the absorption line shape itself may be used to determine the angular product state distribution. This is the result of the products being doppler shifted with respect to the laboratory frame which could, for example, even create two peaks in the absorption line shape if the products recoil in directions towards and away from the probe light. Alternatively, if the products are isotropic, then the peaks will be symmetric in shape.

While line shapes yield dynamic information as described above, the primary dynamic information comes from measuring the product state distributions. In this regard, the mm/submillimeter wavelength direct absorption technique used in the Duffy lab has resolution advantages over other absorption techniques typically used in molecular dynamics research. The technique probes the rotational levels of polar product

molecules. As the rotational levels may be in any vibrational and/or electronic state the full rovibronic state distributions of the products can potentially be resolved. In addition, the ultrahigh resolution is capable of resolving these transitions at a hyperfine level of detail. It also affords the possibility to probe the different spin-orbit states of the products as well as lambda doublet states. All combined, this knowledge will help us determine if the products are forming via the insertion or abstraction mechanisms by seeing if the products are rotationally hot or vibrationally hot, respectively.

II.E. Limitations of Previous Studies

Mutsumi et al. used LIF for probing the ClO products, but LIF has limitations. Using LIF causes excitation of the molecule from the ground electronic state to a higher electronic state and in doing so can cause predissociation. As discussed earlier, in the experiment, Mutsumi et al. performed, they found that predissociation was taking place in vibronic transitions above $v = 3$. This was unfortunate due to the fact that Mutsumi et al. also reported that, energetically, vibrational states for ClO up to $v = 18$ are possible.⁶ The technique of mm-wavelength direct absorption allows us to circumvent this issue because there is no electronic transition taking place and therefore no chance of predissociation. In contrast with the LIF technique, the limitation of mm/sub-wavelength direct absorption experiment lies with the sensitivity.

In an effort to overcome sensitivity issues of the mm/submm-wave technique, the Duffy group has employed high-density ‘slit jet’ nozzles in their experiments. Increasing the number density of product species in the beam directly increases the percent absorption through Beer’s law. Unfortunately, at the densities typically used, the mean

free path is only 2-3 mm, and hence the products rapidly collide with other molecules in the molecular beam. Pinhole nozzles, on the other hand, create molecular beams that are much less dense and hence product signals that are nascent and not tainted by subsequent inelastic scattering. If the concentration in Beer's law is not high, then the alternative to increasing the concentration is to increase the pathlength. This has led the group to explore alternative multipass and other methods for increasing the pathlength through the molecular beam.

A common method for increasing the sensitivity in optical absorption spectroscopy is to increase the effective pathlength with a Fabry-Pérot cavity resonator. A Fabry-Pérot cavity resonator uses two highly reflective mirrors to form a "cavity" where light that leaks in through one dichroic (partially transmissive) mirror can build up in intensity within the cavity. If spherical concave mirrors are used and placed a distance apart equal to their radius of curvature, they form a "confocal geometry" that is particularly effective at building up the light intensity. Two methods that use the confocal method are Cavity Ring-Down Spectroscopy, CRDS, and Cavity Enhanced Absorption, CEAS. The first is a pulsed technique that measures the exponential decay time of photons in the cavity in the presence of an absorbing medium while the second is a similar but continuous wave, CW, a technique that simply detects the increased absorption. The increase in sensitivity stems from the photons having a longer pathlength by repeatedly passing them through the sample which allows for more photons to be absorbed. In a so-called "pass-through" geometry the light then passes out the second dichroic mirror and on to a detector.

While a confocal geometry is desirable, dichroic mirrors like those used in the optical region do not exist in the mm/submm-wave region. Over the years many alternative designs to a conventional pass-through confocal Fabry-Pérot have been proposed by researchers working with mm/submillimeter wavelengths, each with its own technical drawbacks. Below we highlight the work of Braakman and Blake and their efforts to create a high-quality cavity. We then follow it with our own effort in this regard.

Braakman and Blake tested the sensitivity using two different cavity setups with the first being a semiconfocal cavity and then an off-axis semiconfocal cavity with the addition of a wire-grid polarizer.⁴ When the electric field reaches a wire-grid polarizer, the electric field component that is parallel to the wire-grid will cause the electrons to oscillate with the electric field which causes reflection of the electric field or diffraction since there is spacing between the metal wires.⁴ The semiconfocal cavity setup that was used by Braakman and Blake allowed the photons generated by a source to pass through a 50:50 beam splitter and a polarizer, the photons then come into contact with a spherical metallic mirror which reflects the photons back through the polarizer, then into a 50:50 beam splitter to redirect the photons to the detector. Braakman and Blake do note that the two passes through the beam splitter caused a loss of 75% of power and that is without including any power loss caused by the cavity itself.⁴ Figure 9 shows a retroreflected design where the source and detector are on the same side, and Figure 10 illustrates a design that uses an off-axis parabolic mirror to create a type of unfolded pass through Fabry-Pérot cavity, with both semi-confocal designs seen below. In front of both the

photon source and detector are wire-grid polarizers at equal distances which allows the creation of the resonance cavity between the polarizers and the off-axis parabolic mirror.⁴ Since beam splitters are no longer needed, there is less overall power loss which allows for less diffraction loss.⁴

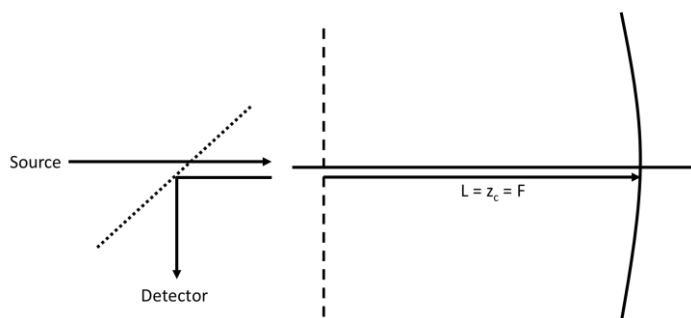


Figure 9. A Semiconfocal Cavity Moving Through a Beam Splitter (Redrawn from Ref. 4).

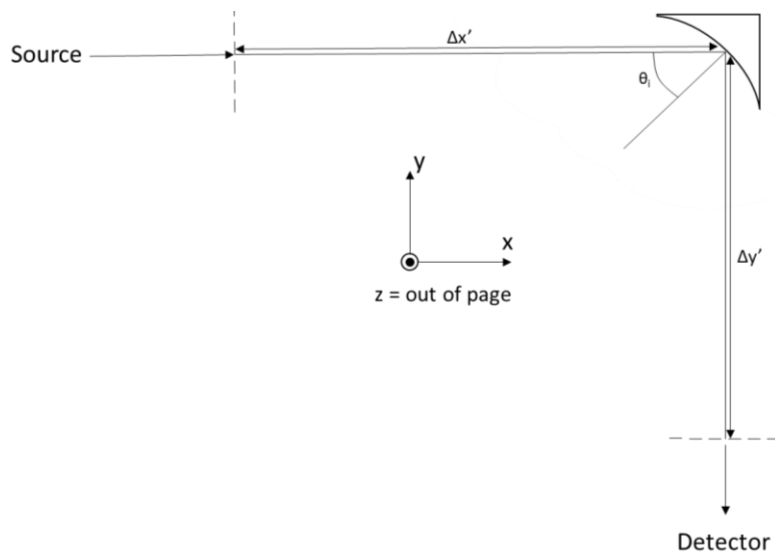


Figure 10. Semiconfocal Cavity But the Photons Move to an Off-Axis Detector (Redrawn from Ref. 4).

To determine the quality of the cavity that is being used, a quality factor (Q) needs to be determined, which can be expressed as:

$$Q = \frac{2\pi L}{\lambda\alpha_m}, \quad (8)$$

where λ is the wavelength of the photons, L is the length of the cavity, and α_m is the sum of the losses at the mirror.⁴ Equation 8 only works for the photon traveling down the length of the cavity once, not a roundtrip which is expected for this type of cavity. To compensate for the factors of a roundtrip, the doubling of the length and the sum of losses is required, which can be seen below:

$$Q = \frac{4\pi L}{\lambda\alpha_{RT}} \quad (9)$$

To find what is called the “loaded Q” which encompasses coupling losses can be determined through spectra from the equation below:

$$Q_L = \frac{\nu}{\Delta\nu} \quad (10)$$

With ν representing frequency and $\Delta\nu$ being the width of the cavity mode.⁴ Braakman and Blake also showed the relationship of the Q factor and the ringdown time (τ) since this setup can be related to cavity Ring-down spectroscopy and to find the effective length (L_{eff}) using the equation below:

$$L_{eff} = \tau c = \frac{Q\lambda}{2\pi} \quad (11)$$

As stated earlier, determining the theoretical Q factor requires knowing the sum of all cavity losses. Braakman and Blake breakdown the main issues that can cause cavity loss with wire-grid polarizers which include the material/metal that is being used. If metal is used, then the metal will have cavity losses with respect to the resistance of the metal since electrons will need to move in the direction of the photons that interact with it. The spacing and circumference of the wires also come into effect where more spacing between the wires can cause less reflectivity, and the smaller circumference of the wires gives a more considerable effective loss to resistance.⁴ Having these factors in mind allows the fabrication of a Fabry-Pérot cavity with a large Q-factor.

As mentioned above, the Duffy research group has fabricated a conventional confocal resonator that focuses the light into a beam waist instead of the semiconfocal cavities used by Braakman and Blake. The Duffy lab uses two spherical focusing mirrors which are separated from each other by a varying length which is adjusted using a picomotor. This is so we can adjust the length to the correct distance between the two focusing mirrors to center the cavity mode to the line frequency being probed. This is because the cavity mode is frequency-dependent, so any change in frequency must have a change in the length of the cavity, which is performed by moving the mirrors until the transmitted power is maximized. Unlike the Blake setups with a separate wire-grid polarizer, the Duffy research group designed two spherical mirrors out of the wire-grid polarizers. This was done by using the photoresist technique, which allows us to place a patterned coating onto the mirrors and then have FeCl_3 to etch the design.

CHAPTER III

EXPERIMENTAL SETUP

III.A. General Setup for the Experiment

Figure 11 below depicts the layout of the mm/submm-wave experiment used in the Duffy lab. A single molecular beam is generated by a slit or pinhole nozzle attached to a rotatable “arm” inside the chamber which allows the possibility of changing the direction/angle of the molecular beam. The slit and pinhole nozzles release a pulse of gas, with the amount pulsed into the chamber being dependent on the stagnation pressure (backpressure) behind the nozzle which is monitored with a capacitance manometer pressure sensor.

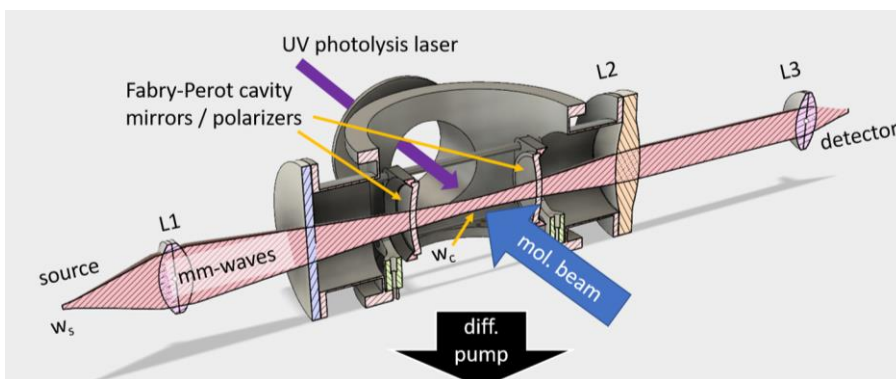


Figure 11. Cutaway View of Duffy Lab Mm/Submillimeter-Wave Molecular Beam Setup with Conventional Pass-Through Confocal Fabry-Pérot Resonator. The Red Beam Indicates the mm/Submm Wave Radiation, the UV Radiation Indicated by the Purple Arrow.

As discussed above, we use the PHOTOLOC technique where a molecular beam of generated ozone is mixed with carbon tetrachloride and a carrier gas, described below. The reactive O(¹D) atoms are generated by photolysis of the ozone with 266 nm UV light from a pulsed Nd:YAG laser. The carrier gas used has initially been Argon but later Helium. What prompted the switch was Helium's higher slip velocity (a more significant difference in velocity between the two particles in question) which reduced ozone clustering whereas Argon was causing considerable clustering of ozone and is described below. The laser pulse timing is matched to the pulsing frequency of the slit nozzle and is delayed coinciding with the arrival of the molecules in the center of the chamber.

III.B. Ozone Generation and Gas Inlet Manifold

Ozone is generated in the Pacific Ozone (Model G11) generator that is in a hood. The procedure to set up the ozone generator is in accordance with the set-up procedure found in the manual. Dry O₂ is passed through the generator with a flow rate around 10 Standard Cubic Feet Per Hour (SCFH). Once the flow rate has been established, the ozone generation is set to about 70-80% for 30-40 minutes. The ozone generated is then captured on silica gel beads located in a cold finger, and that is kept at -78 °C via a dry ice/acetone bath. As ozone begins to be captured on the silica gel, a purple hue appears. While this confirms the presence of ozone, it is not quantitative. Any excess ozone flows into a 1ft x 3" diameter metal pipe containing Carulite 200®, an ozone destroying catalyst mixture of manganese dioxide and copper oxide catalyst which destroys the ozone and the resulting molecular oxygen is exhausted into the hood.

Ozone is explosive and exceedingly harmful to one's health so precautionary steps need to be taken. Neat ozone can explode if it is in a liquid state and allowed to evaporate. For this reason, ozone is instead trapped onto the surface of silica gel beads which prevents it from pooling. To prevent molecular oxygen from condensing along with the ozone, we used a dry ice/acetone bath since it maintains a temperature of $-78\text{ }^{\circ}\text{C}$, cold enough to trap ozone but not molecular oxygen. It is crucial not to use liquid nitrogen for ozone generation, doing such will condense both ozone and molecular oxygen onto the silica gel which would pose an additional explosion hazard. While our set up should mitigate the risk of explosions, anytime ozone is generated, a blast shield is placed in front of the Dewar that holds the cold finger and the hood sash is lowered. Any work around the ozone generator while it is operating required us to wear face shields. Fortunately, we have never encountered an issue with ozone exploding in our laboratory.

Ozone also poses a health hazard. Exposure to 100 ppm of ozone for 1 minute can be deadly.²¹ As previously stated, we use a metal pipe containing Carulite 200® to remove any excess ozone that is not captured on the silica gel and prevent it from escaping into the hood or into the room. This has the added benefit of protecting the vacuum system the building might be using and the hood because ozone is a strong oxidizing agent.

As previously stated, we originally followed the operating directions of the manual that came with the Pacific Ozone G11 generator but a document explaining another groups ozone generation was discovered with similar steps.²⁴ The principle difference being that they used a heating element to heat the silica gel prior to any ozone

generation, under vacuum. This allowed for any water on the silica gel to evaporate off, allowing for more ozone to be captured during the experiment. Their setup also used isopropyl alcohol/dry ice bath instead of an acetone/dry ice bath. They mention that the reason for this was isopropyl alcohol has a lower volatility, so it's a lower ignition hazard in the event of an explosion, and it has a lower vapor pressure than acetone, therefore should last longer in the hood.²⁴

After ozone is generated, it is introduced to the experiment by opening the output of the cold finger to the experiment and flowing argon and/or helium carrier through the ozone covered silica gel. The ozone and carrier gas mixture then flows through about 10 meters of Teflon tubing until it reaches the experimental chamber. Teflon is used because it will not react with ozone. Originally, to determine if we have generated ozone, we can tune the mm-wave synthesizer to a known ozone transition and run an absorption experiment which can be seen below in Figure 12, you can see an ozone absorption signal with a loss of absorption in the center. The loss of absorption is due to the laser dissociating the ozone into atomic diatomic oxygen.

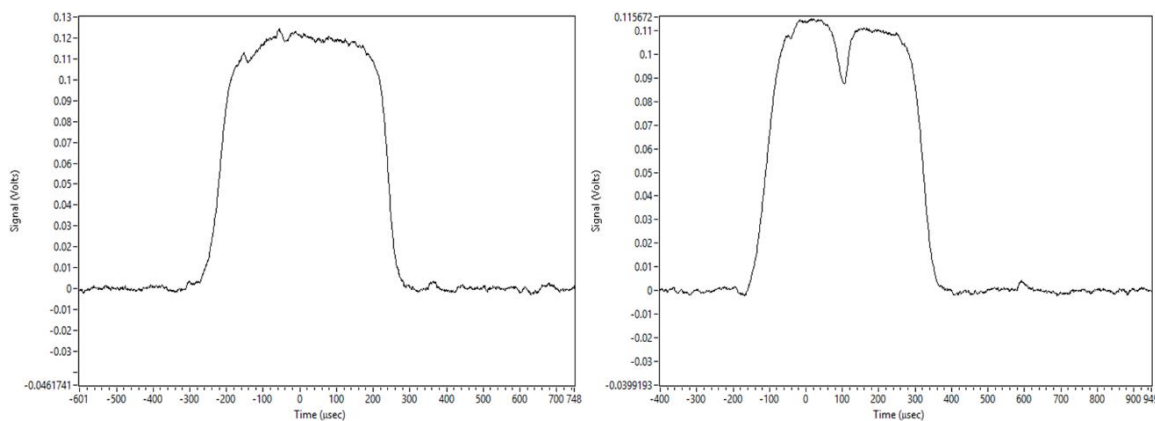


Figure 12. O₃ Absorption Signal with a Hole Generated by the 266 nm Output of a Nd:YAG Laser. Time is on the X-Axis, Signal in Volts is on the Y-Axis. The Left Spectra Shows an Ozone Absorption Signal Without the Laser Firing, the Right Spectra Shows the Same Signal But the Nd:YAG Laser is Firing and Causing Dissociation of the Ozone, Indicated by the Hole/Dip in Center of the Signal. Center Frequency is 164951.8200000. Transitions are $N = 7 \leftarrow 6$, $K_{-} = 1 \leftarrow 0$, $K_{+} = 7 \leftarrow 6$, $\nu = 0 \leftarrow 0$.

Unfortunately, this method of detecting the presence of ozone was not readily quantifiable without assumptions about the molecular beam rotational temperature and effective pathlength. It also was not continuous and required repeatedly retuning the mm-wave cavity to ozone frequencies just to make sure ozone was still present. More recently, a second method to determine and quantitate ozone concentration after it was generated was to have the ozone gas pass through a custom fabricated 1 cm pathlength fiber-optic coupled Teflon gas cell, monitored with an Ocean Optics® UV/Vis spectrometer. This now allows us to continuously monitor the concentration of ozone as it reaches the experimental chamber, not only giving us a second independent method to determine if ozone is generated, but also forgoing the need to stop the current experiment to determine if ozone is still present. The location of the spectrometer is just before the

gas enters the main experimental chamber and can be seen in a simplified view of the gas inlet manifold in Figure 13 below.

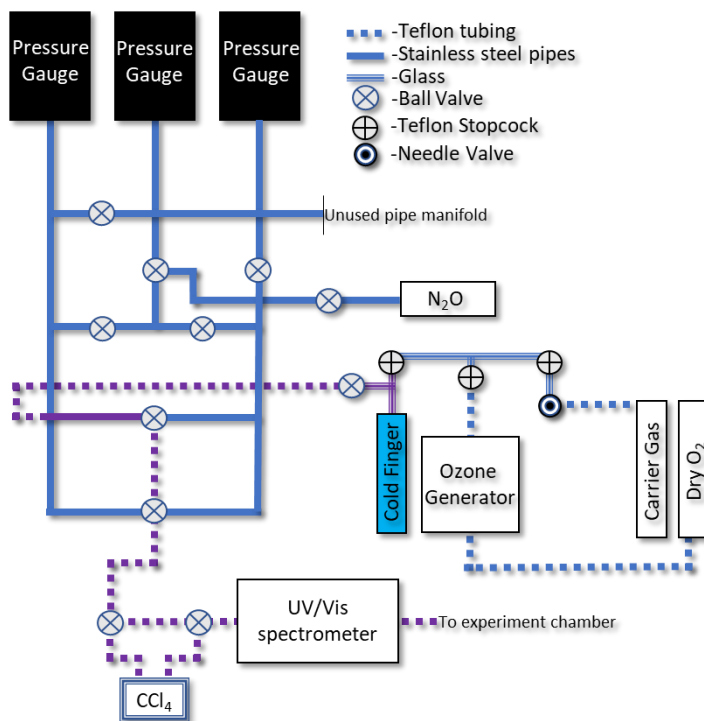


Figure 13. Simplified Gas Inlet Manifold. The Purple Indicates the Route the Ozone Gas Takes to Get to the Experimental Chamber.

A bottle is filled with 20 to 30 mL with carbon tetrachloride (so this step does not have to be repeated). The bottle containing carbon tetrachloride is placed under vacuum until the pressure is below the vapor pressure of carbon tetrachloride (93.1 torr at room temperature) and then ozone can be allowed to flow into the bottle. A panel was made to control the mixing of ozone and carbon tetrachloride, which can be seen in Figure 14.

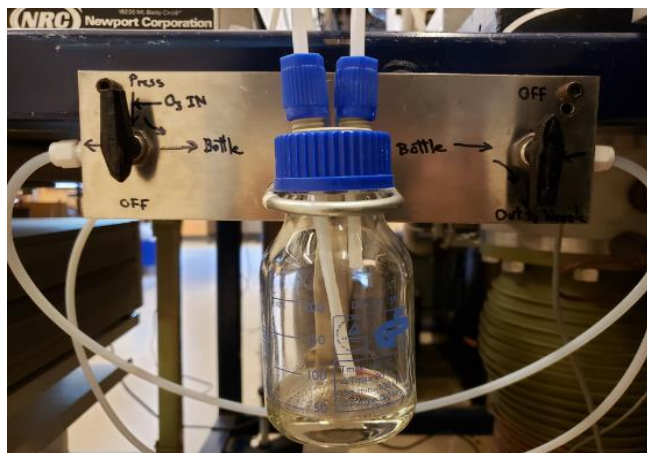


Figure 14. Carbon Tetrachloride Setup.

Ball valves allow the ozone to bypass the bottle completely if desired. This allows the possibility to pulse just ozone into the chamber to perform a test scan to see if the experimental set up is aligned and working correctly. The bottle is Duran and the top screws off and on to add chemicals as needed.

Once the ozone and carbon tetrachloride vapor are mixed, the slit or pinhole nozzle is turned on and starts pulsing the gas into the main chamber. Helium is then allowed to flow into the mixture as a carrier gas. The Fabry-Pérot cavity is then tuned to a known rotational frequency of ozone. Once the cavity is set, the mm/submm-wave synthesizer is stepped through frequencies close to the rotational transition frequency of interest and the transient absorption signals at each frequency are acquired from the mm/submm-wave detector on an oscilloscope and then transferred to a computer. This data acquisition system is controlled by custom LabVIEW data acquisition software. When searching for ClO in excited vibrational states the same procedure is used.

After probing many efforts to probe the rovibrational distribution of ClO, we tried to synthesize nitric oxide (NO) by reacting O(¹D) that was dissociated from ozone and react it with nitrous oxide (N₂O). Ozone was generated by the same procedure that we used for generating ozone for ClO. Nitrous Oxide was already in a tank that is connected to the same gas inlet manifold that we used to pulse the ozone into the chamber by a cylinder regulator. The N₂O was allowed access into the cold finger with the ozone to assist with the mixing. While there is no indication that this make the ozone any more of a explosion hazard, and N₂O should not condense onto the silica gel, caution should still be taken. Once the ozone and the nitrous oxide vapors mix, the nozzle was turned on.

CHAPTER IV

EXPERIMENTAL DATA

IV.A. Nitrous Oxide Signal and Effect of Fabry-Pérot Cavity

Nitrous oxide (N_2O) is a convenient, inexpensive polar gas we use to test the experimental setup and cavity. A scan is seen in Figure 15 below, on the z-axis is the absorption signal (volts), y-axis shows Frequency (MHz), and Time (μsecs) on the x-axis.

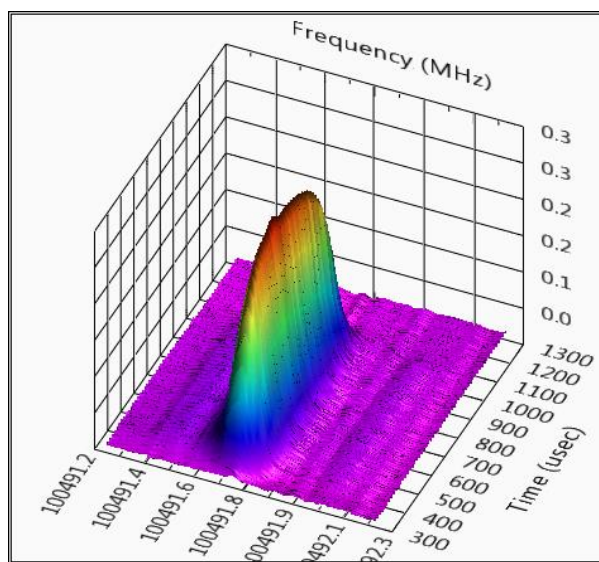


Figure 15. Absorption (V) of N_2O with the Z-Axis is the Absorption Signal (Volts), Y-Axis Shows Frequency (MHz), and Time (μsecs) on the X-Axis at a Center Frequency of 100491.740000 MHz. Transitions Were $N = 4 \leftarrow 3$, $J = 4.5 \leftarrow 3.5$, $K = 0 \leftarrow 0$, $\nu = 0 \leftarrow 0$.

The horizontal axis gives the frequency in MHz while the receding axis allows us to see when in time, the gas pulse is absorbing the power and how much. When the Fabry-Pérot cavity is added to the experiment, the signal intensities increase dramatically

and change in shape. Figure 16 below, shows the same rotational transition of N_2O but now with the cavity present. A discussion of the new cavity induced line shape is the subject of recent studies in the lab. The full analysis is complicated, and for our present purposes, beyond the scope of this thesis. For clarity, the signal in Figure 16 is inverted from that of Figure 15. The crater in the volcano-shaped signal is due to the absorption while the rim of the crater is due to a dispersion effect, described below.

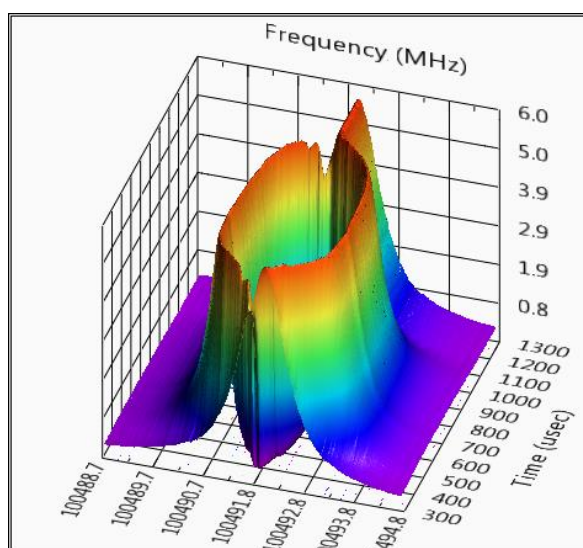


Figure 16. Absorption and Dispersion Signal of N_2O in the Presence of the Fabry-Pérot Cavity Tuned to be Coincident With the Line Center Frequency of 100491.740000 MHz. Transitions Were $N = 4 \leftarrow 3$, $J = 4.5 \leftarrow 3.5$, $K = 0 \leftarrow 0$, $\nu = 0 \leftarrow 0$.

Briefly, the line shape can be understood as follows. At early and late times, in the figure above, i.e., when no gas molecules are present in the cavity, the signal represents the power spectrum coming through the cavity. This reflects a normal cavity mode resonance for a Fabry-Pérot cavity ($Q \approx 74,000$). When the gas arrives after about 300 μsec , the cavity mode bifurcates into two new resonances that appear as off-resonant

wings at approximately ± 1 MHz from line-center. What's startling is that the intensity of the power through the cavity this far away from line-center (lines are normally ~ 100 kHz wide) is about the same as the molecule-free cavity resonance. In a nutshell, at ± 1 MHz the dispersion phase shifts the mm-waves experience going through the gas results in both positive and negative half-cycle phase shifts in the mm-waves as compared to what the molecule-free mm-wave beam would experience along the same path. Because a Fabry-Pérot cavity has resonances when the mm-wave field has a node at the mirror, a half-cycle phase shift ends up with nodes at the cavity mirrors and hence corresponding cavity resonances, the wings in Figure 16. Additionally, since the mm-waves are far off resonance the molecules absorb very little power at these wing frequencies. Conversely, when the mm-waves are tuned to transition line-center, all the mm-wave power is absorbed by the molecules, the result is fully saturated absorption at line-center. The signal in Fig. 15 is also particularly strong because we were using a neat beam of N_2O .

Going forward in this thesis, the relevant point of the discussion above is that the cavity has dramatically enhanced our signals. The integrated area of the signal in Figure 16 is a factor of 70-fold larger than that of a normal cavity-free line like the one in Figure 15. Our hope and a central goal of this work, is to use this new found signal enhancement to look for smaller ClO product signals in excited vibrational states that we suspect are present but until now we have lacked the sensitivity to observe without using excessive gas flows that increase product collisions and undermining the nascent distributions we wish to record. The result below, show mixed success in this regard.

IV.B. ClO Product Signal

Once the studies characterizing the behavior of the new Fabry-Pérot cavity were complete we moved onto probing ClO as the product in the reaction of $O(^1D) + CCl_4$ with the hope as just mentioned above that the increased cavity enhanced sensitivity would allow us to detect faint products signals. For the ground vibrational state, we observed rotational state transitions from $J' \leftarrow J'' = 5.5 \leftarrow 4.5, 6.5 \leftarrow 5.5,$ and $7.5 \leftarrow 6.5,$ the last of which is shown below to demonstrate the hyperfine resolution possible with our experiment with the peaks representing Λ -doublets. As a radical, ClO has a $^2\Pi_{3/2}$ ground state. Each peak of the Λ -doublet represents a different projection of the unpaired electron's orbital angular momentum on the molecule's axis. Studies on some other molecular systems have been able to ascribe differences in doublet peak intensities to the type of molecular orbital being broken in the reaction.^{29,30} When a π -type bond cleaves, the unpaired electron is left in a p-like orbital perpendicular to the plane of rotation of the molecule. Likewise, if a σ -type bond from two overlapping axially aligned p_z orbitals is broken, the final p-like unpaired electron orbital can be in the plane of the tumbling product molecule.^{29,30}

Such a preference for one Λ -doublet peak over the other is not visible in Figure 17. This could either indicate that no preference exists, or that in the process of dissociating any initial preference is scrambled through intra-molecular fields, a slow dissociation or simply through subsequent collisions in the beam. More examples are given in the figures in the appendix and even some that show a single broad peak. At this point we need to do some more modelling to know if this is an artifact of the Fabry-Pérot

cavity or a reflection of dynamics. Going forward we also need to systematically look for ClO products in the excited $^2\Pi_{1/2}$ spin-orbit state. Λ -doublet splitting is significantly larger in this state which might help preserve any nascent preference for one doublet peak over the other.

The remaining scans are shown in appendix A. Once O(1D) and carbon tetrachloride react to form ClO at the intersection of the UV laser and molecular beam, the molecules start colliding into each other and by the time they reach the center of the mm-wave cavity a single molecule might have collided with other molecules 3 to 4 times. This energy transfer/loss is enough to allow the rotational states of ClO to be thermalized.

We decided to probe higher vibrational states but showed no new results. A possibility as to why might be that particle collisions could be causing the rotational and vibrational distributions to be relaxed. To determine if the collisions were causing the rotational and/or vibrational distributions to be relaxed, we moved the slit nozzle closer to the Fabry-Pérot cavity beam waist. Once performed, there was a small absorbance peak for ClO in the $v=3$ vibrational state, which can be seen in Figure 20. To date we have probed for signals in vibrational levels 1-8 for ClO but have only found products in the ground state, with the one exception of a signal in the 4th excited vibrational state. This is surprising given that the possible vibrational states accessible to the ClO in this reaction have been reported to be as high as the $v=18$.⁶

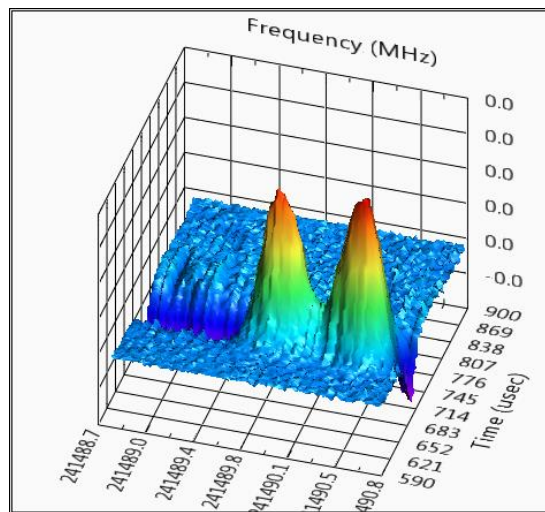


Figure 17. Absorption Signal for ClO Product Molecules in the Ground Vibrational State. The Hyperfine Transition at the Center at 241489.781700 MHz is $N = 6 \leftarrow 5$, $v = 0 \leftarrow 0$, $J = 6.5 \leftarrow 5.5$, $F = 8 \leftarrow 7$. The Left Peak Shows the Transition $\Lambda = 1 \leftarrow -1$, the Right Peak Being $\Lambda = -1 \leftarrow 1$.

In addition to moving the nozzle we also tried a pinhole nozzle to create a much lower density molecular beam in the hope that there would be less interference caused by the bumping of molecules. The slit nozzle produced substantial absorbance peaks for ClO in the ground state in Figure 18 but using the pinhole nozzle we can only see a faint absorbance peak in Figure 19 that is smaller than what is seen in figure 18, which can indicate either we are not producing ClO which seems unlikely seeing how the experimental setup and procedure has not changed, less reactants are being pulsed into the chamber, therefore producing less product, or there are fewer collisions happening between the molecules in the beam and hence the rotation distribution has not been thermalized. The work cited in the introduction by Matsumi and Shamsuddin suggests nascent rotational temperatures ranging from 900 ± 100 K to 2050 ± 60 K. Ironically, our desire to see nascent products might have resulted in nascent rotational temperature

distribution that are too high, keeping population out of the low rotational states we can access with our mm-wave sources. Unfortunately, we only have sources that can take probe rotational levels up to about $J' = 8.5$. Thermalizing rotational collisions would enhance our signals by moving population down into levels we can probe. The upshot of all of this is that while the cavity may have helped us see smaller signals the use of the pinhole resulted in rotational populations in the states we can probe that are too low to detect well.

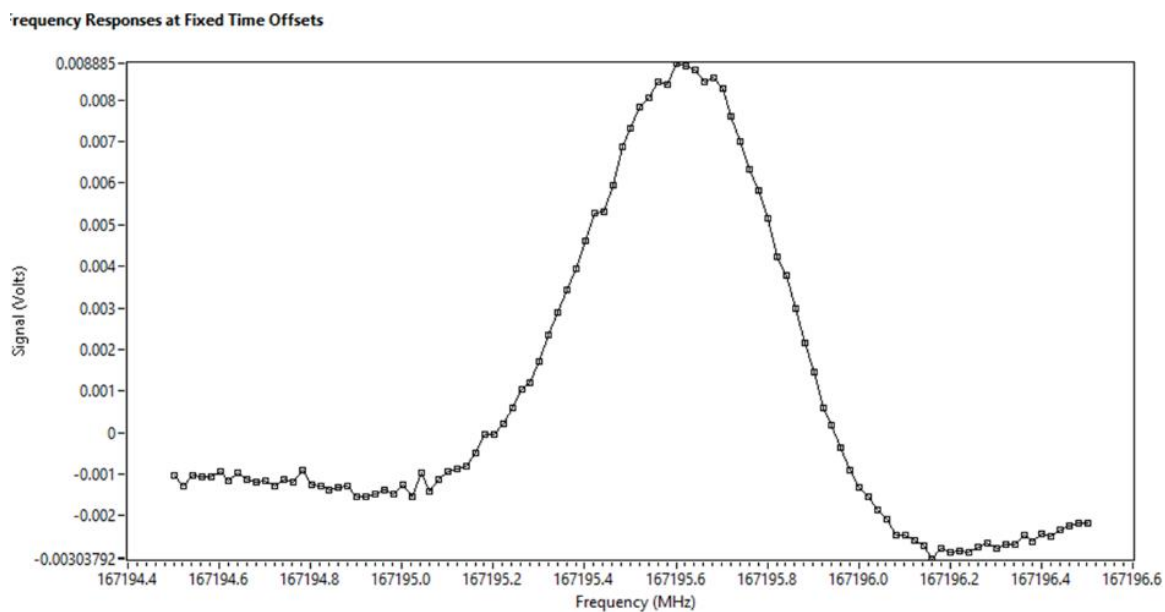


Figure 18. Absorption Signal for ClO While Using a Slit Nozzle With a Center Frequency of 167195.838000 MHz, Transitions Were $N = 4 \leftarrow 3$, $A = -1 \leftarrow 1$, $v = 0 \leftarrow 0$, $J = 4.5 \leftarrow 3.5$, $F = 6 \leftarrow 5$.

Frequency Responses at Fixed Time Offsets

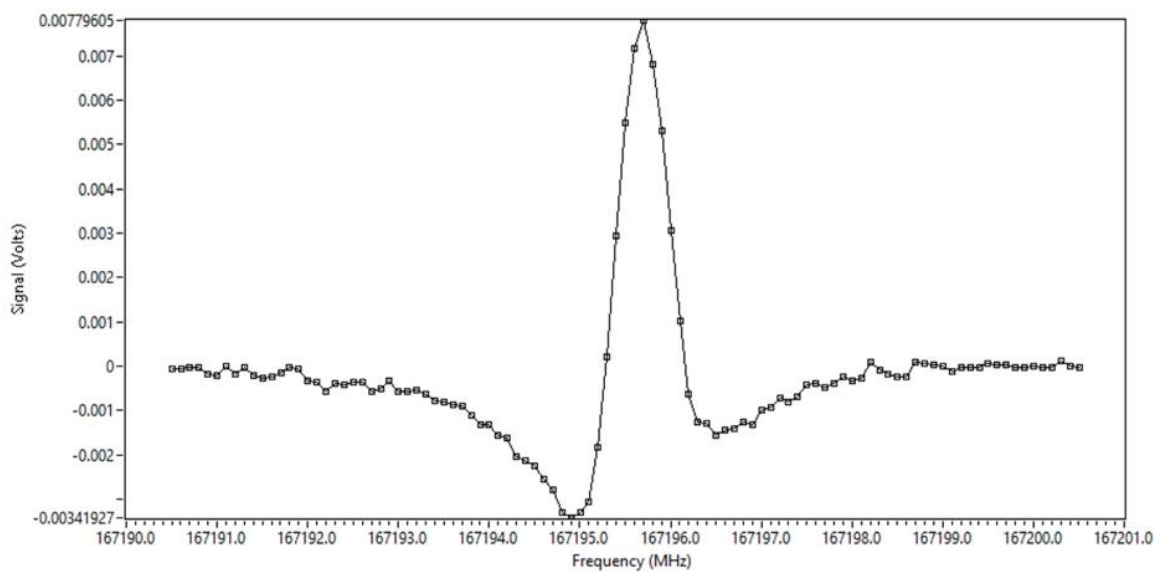


Figure 19. Signal for ClO While Using a Pinhole Nozzle With a Center Frequency of 167195.838000 MHz, Transitions Were $N = 4 \leftarrow 3$, $\Lambda = -1 \leftarrow 1$, $v = 0 \leftarrow 0$, $J = 4.5 \leftarrow 3.5$, $F = 6 \leftarrow 5$.

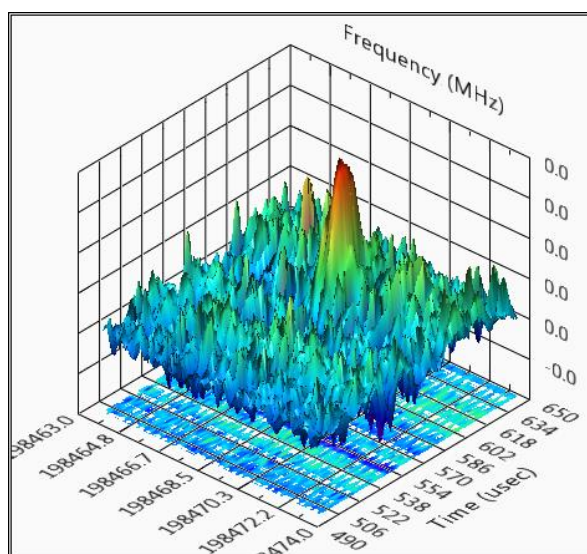


Figure 20. Absorption Signal for a Vibrationally Excited ClO Product Signal With a Center Frequency of 198468.5256 MHz, Transitions Were $N = 5 \leftarrow 4$, $\Lambda = -1 \leftarrow 1$, $v = 3 \leftarrow 3$, $J = 5.5 \leftarrow 4.5$, $F = 6 \leftarrow 5$.

IV.C. NO Products

We decided to try another experiment involving nitrous oxide reacting with $O(^1D)$ to form nitric oxide. All scans have been performed in the ground vibrational state and with a pinhole nozzle. The figures below show the absorption signal, determined by the open square points connected by black lines, the line frequencies, shown in green, were determined by Varberg and his research group.^{15,17} I have shown the most prominent signals below in Figures 21 and 22, the remaining signals are shown in Appendix B.

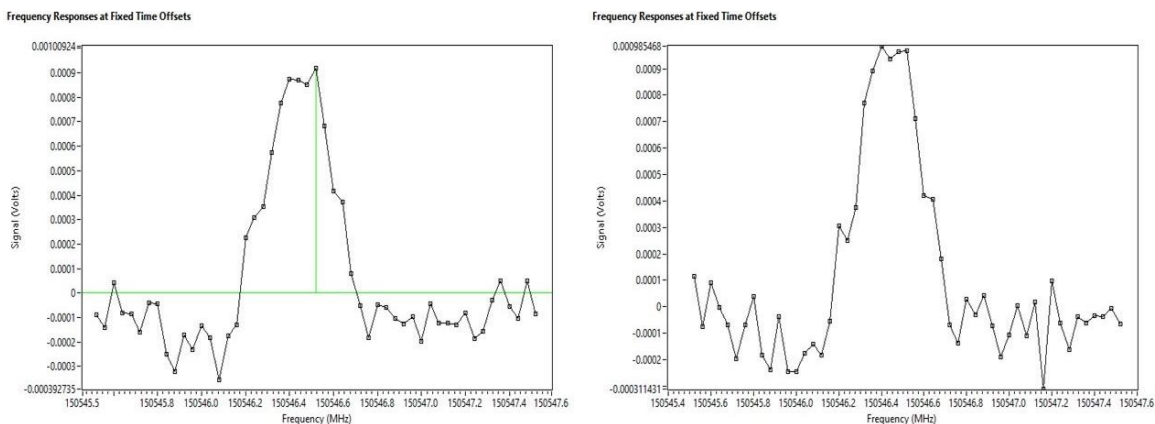


Figure 21. Absorption Signal for NO With a Center Frequency of 150546.520000 MHz, Transitions Were $N = 2 \leftarrow 1$, $\Lambda = 1 \leftarrow -1$, $v = 0 \leftarrow 0$, $J = 1.5 \leftarrow 0.5$, $F = 2.5 \leftarrow 1.5$.

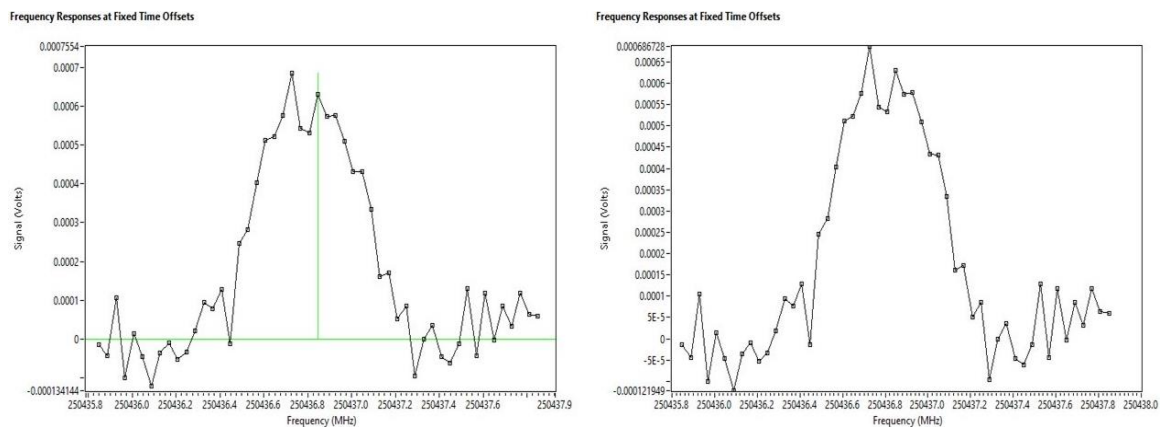


Figure 22. Absorption Signal for NO With a Center Frequency of 250436.848000 MHz, Transitions Were $N = 3 \leftarrow 2$, $A = 1 \leftarrow -1$, $v = 0 \leftarrow 0$, $J = 1.5 \leftarrow 0.5$, $F = 3.5 \leftarrow 2.5$.

We chose nitrous oxide because it is readily available and because it is considered a greenhouse gas and unlike chlorofluorocarbons, nitrous oxide was not regulated by the Montreal protocol.

CHAPTER V

DISCUSSION OF O(¹D) + X (CCl₄, N₂O) REACTIONS

V.A. O(¹D) + CCl₄ Reactions

As discussed previously, Matsumi and Shamsuddin's research was used as a guide for this experiment because of their work on determining the relative populated vibrational states of chlorine monoxide.⁶ Upon performing our experiments we have found products primarily in their ground vibrational states, except for one small absorption signal in the v=3 vibrational level. This is at odds with the vibrationally inverted results of Matsumi and Shamsuddin's which found populations increasing with vibrational level. Our results are also at odds with the energetics that suggest the possibility of high vibrational excitation. As mentioned earlier, ClO vibrational levels up to v=18, should be possible. Trajectory calculations on the similar reaction of H + CCl₄ → HCl + CCl₃ show that Polanyi Rules for a Light-Heavy-Heavy (L-H-H) reaction should be observed and that HCl should be vibrationally excited above the ground vibrational level.^{26,27} While we have not found similar trajectory calculations on O(¹D) + CCl₄ in the literature, it does have the same L-H-H motif, albeit with an oxygen atom that is significantly heavier than H but still lighter than Cl. The entrance channel for O(¹D) should also be barrierless. All of this suggests that ClO should likely be found vibrationally excited, at least above v=0.

The two different experimental approaches may help explain the different outcomes. Matsumi and Shamsuddin performed their experiments using LIF along with a reaction flow cell. In contrast, we used the PHOTOLOC method in a single molecular beam. While the number densities in both experiments should be roughly comparable, the initial translational temperature distribution of the reactants is much smaller in our molecular beam, a few Kelvin in our case, versus room temperature in the flow cell.

Although the translational temperature of the reactants is different in the two experiments, it is worth pointing out that the relative kinetic energy between the O(¹D) and CCl₄ is largely dominated by the high initial velocity of the O(¹D) atom following photolysis. The initial thermal translational energy difference between experiments is small compared to this. Similarly, in the LIF work, the photolysis wavelength of 248 nm was shorter than our 266 nm, leading to slightly higher O(¹D) atoms velocities (about 2500 m/s versus about 2100 m/s).^{6,22,25} It is unlikely that these small starting energy differences can account for the different vibrational distributions.

A more likely explanation for the difference between the LIF flow cell work and our own, is that the much lower temperatures of the molecular beam may have led to clustering of the reactant molecules. This effect would be exacerbated for the slit nozzle experiments. To test this, I took scans with and without helium as a carrier gas to see if there was a difference. Helium, being significantly lighter has a “slip velocity” in the molecular beam, resulting in extra gas collisions that help break up clusters. Unfortunately, we only found that the signals became weaker or that no signals were observed at line frequencies where previous signals were observed.

We also considered the idea that O_2 existed as an impurity in our molecular beam as a remnant from the ozone generation process. If present, ClO might have vibration to vibration energy transfer with O_2 and vibrationally relax. Although previous theoretical research has shown that little to no vibration-vibration energy transfer is expected between diatomic oxygen and chlorine monoxide, we reran the experiments with the cold finger that contained ozone was evacuated to about 15 torr to try and remove any excess diatomic oxygen.¹⁰ Still no vibrationally excited chlorine monoxide signals were observed.

We tried switching out the slit nozzle to a pinhole nozzle as previously stated but again, no real changes were observed except for signals being slightly weaker (experiments were tried with and without helium). Instead of changing the molecular beam density, we tried changing the location and geometry of the molecular beam.

Collisions are bound to happen, so we tried moving the nozzle of the molecular beam to boarder the beam waist of the Fabry-Pérot cavity. This would hopefully allow for less time for the particles to collide with each other since they have less of a distance to travel. Alas, no signals in excited vibrational states were detected. We tried changing the geometry of the molecular beam to approach from a 45-degree angle concerning the mm/sub-mm waves and the Fabry-Pérot cavity with no results. The last change in geometry we tried was having the molecular beam come from the top of the chamber (if the mm/submm waves are moving towards the positive y-axis and the laser moving towards the positive x-axis, the molecular beam would move towards the negative z-axis). This idea came with the benefit of having an adjustable arm that allowed for a

quick change in the distance the particles would have to travel, allowing us to see any rovibronic relaxation in real-time. This would have been done by adjusting how much the arm would extend into the main experimental chamber, therefore the distance the molecules would have to travel before they entered the cavity but sadly this modification had no results, even in the ground vibrational state, so we moved back to our original geometry with the molecular beam being counter propagated with the laser.

Separate work in Duffy research group on the photodissociation of ClO_2 to produce $\text{ClO} + \text{O}$, observed ClO vibrational states up to $v=7$ being populated. It is through this work that we know what the rotation transition frequencies are for the excited vibrational states of ClO . In those experiments the ClO vibrational distribution was inverted, and UV wavelength dependent. In those experiments there were clearly observed effects of rotational state thermalization with little vibrational state quenching.²³ It is because of this prior work that we expected to detect the vibrationally inverted products as observed by Matsumi and Shamsuddin.

Another possibility why we see no signals are maybe the products are coming out rotationally hot, or at higher rotational states than what we can scan for with the frequency domain available to our sources (50 GHz – 660 GHz). Matsumi and Shamsuddin's showed the other chlorofluorocarbons reactions had rotational temperatures ranging from 900 ± 100 K to 2050 ± 60 K depending on the type of reaction, carbon tetrachloride with $\text{O}(^1\text{D})$ rotational temperature was not reported because they could not determine the cause of excess fluorescence that was occurring in the reaction cell and decided best not to report the data.⁶

Let us look at the one signal in the $v=3$ vibrational state. Maybe this scan is indicating we are generating particles in the higher vibrational states but there are so few particles that almost no absorption can be seen. This is interesting because the Fabry-Pérot cavity we have installed is extremely sensitive, so sensitive we were able to see the magnetic dipole allowed transitions of diatomic oxygen (we confirmed this by using a magnet to change the splitting) as can be seen in Figure 44 in Appendix C. The magnetic dipole moment is about 1000 times weaker than an electric dipole moment, so why we see that but no excited chlorine monoxide particles in excited vibrational states is interesting. In the end, after all these efforts to find vibrationally excited ClO, no new signals were detected. We decided to switch to a different reaction than we could perform readily with the reagents we had in the lab, $O(^1D)$ with nitrous oxide to produce nitric oxide.

V.B. $O(^1D) + N_2O$ Reactions

Nitric oxide studies were attempted by a previous graduate student in Dr. Duffy's lab, Mariam Fernanders.²⁰ Mariam did not find any nitric oxide products in her experiments so I was curious to see if we could see the nitric oxide products with our new Fabry-Pérot cavity setup. Using essentially the same setup and experiment used for chlorine monoxide, we searched for nitric oxide and found nitric oxide absorption signals with relative ease. Although, I am close to the limit of the data I can obtain because most available data for nitric oxide's rotational states are outside of our frequency domain and therefore could not be investigated. We also could not find any previous research or data indicating any rotational states in higher vibrational states that could be used within our

frequency domain but researchers have indicated that nitric oxide located in the stratosphere might be found to have nascent populated excited vibrational states as high as $v=14$.¹⁹ The more defined absorption peaks of NO can be seen above in figures 21 and 22 and the rest of the data collected can be seen in Appendix B at the end of this thesis.

V.C. Conclusions

The purpose of this thesis was to measure the rotational, vibrational, translational, and electronic states of chlorine monoxide produced by the reaction $O(^1D)$ and carbon tetrachloride by direct mm-wave absorption to try and deduce the reaction dynamics taking place between the reactants. The experiment revealed products but only in the ground vibrational state; no products were seen in any excited vibrational state except for one small absorption signal in the $v=3$ vibrational state but we expected more ClO products to be in excited vibrational states due to previous research by Matsumi and Espinosa-garcía.^{6,26} Other research²⁸ has indicated that the products might be observed in lower rotational states as we increase the vibrational distribution. If so, we might be able to probe these states since the lower rotational states fall within our frequency domain of 50 GHz to 660 GHz.

With that said, we might not see any signals if the product is in too high of a vibrationally excited state. We can only probe up the $v=8$, any vibrational levels $v>8$ we lose the ability to see where to probe for the transitions. To find these frequencies would require long frequency scans that would take a substantial amount of time to perform and since the Fabry-Pérot cavity is needed to observe these signals. This means anytime a change in frequency occurs we would need to change the length of the cavity so we

would need to develop a method to synchronously control the cavity length as the frequencies change. To determine if we could see other products, we also searched for the product signals of nitric oxide produced by the reaction $O(^1D)$ and nitrous oxide and found absorption peaks for nitric oxide in the $v=0$ vibrational level.

Future work in finding the rovibronic distribution of ClO signals can be performed but will need further optimization. Since we have absorption peaks for ClO using both the slit nozzle and pinhole nozzle but only in the ground vibrational state and one excited vibrational state, switching to a different gas, like chlorine gas instead of carbon tetrachloride, might help expedite the process of finding the rovibrational distribution of ClO. Experimentally, we now have a way to quickly add liquids and solids to the experiment with ease which broadens our scope of possible reactions and our experiment sensitivity has been massively improved thanks to the Fabry-Pérot cavity we now have installed. Further work in finding the frequency transitions for the rotational states in $v>8$ vibrational states might be a time-consuming process but may lead us to finding more signals in the excited vibrational states and once done, will help unravel the molecular dynamics of the $CCl_4 + O(^1D)$ reaction.

REFERENCES

1. Zhang, J.; Lee, Y. T. Crossed Molecular Beam Study of the Reaction $\text{Cl} + \text{O}_3$. **1997**, *5639* (97), 6485–6495.
2. Strahan, S.; Douglass, A. Decline in Antarctic Ozone Depletion and Lower Stratospheric Chlorine Determined from Aura Microwave Limb Sounder Observations. *Geophys. Res. Lett.* **2018**, No. 45, 382–390.
3. Fernandez-Alonso, F.; Bean, B. D.; Zare, R. N. Measurement of the $\text{HD}(v' = 2, J' = 3)$ Product Differential Cross Section for the $\text{H} + \text{D}_2$ Exchange Reaction at 1.55 ± 0.05 eV Using the PHOTOLOC Technique. **1999**, *111* (3), 1022–1034.
4. Braakman, R.; Blake, G. A. Principles and Promise of Fabry – Perot Resonators at Terahertz Frequencies. **2011**, *063102*, 1–11.
5. Zare, R. N.; Rettner, C. T.; Lubman, D. M. How Isolated Are Molecules in a Molecular Beam? *J. Chem. Phys.* **1982**, *86*, 1129–1135.
6. Matsumi, Y.; Shamsuddin, S. M. Vibrational and Rotational Energy Distribution of ClO Produced in Reactions of $\text{O}(^1\text{D})$ Atoms with HCl, CCl_4 , and Chlorofluoromethanes. *J. Chem. Phys.* **1995**, *103* (11), 4490–4495.
7. Matsumi, Y.; Shamsuddin, S. M.; Kawasaki, M. Laser-Induced Fluorescence Detection of ClO Radicals at 167–180 Nm. *J. Chem. Phys.* **1994**, *101* (9), 8262–8263.
8. Matsumi, Y.; Tonokura, K.; Kawasaki, M.; Tsuji, K.; Obi, K. Dynamics of the Reactions of $\text{O}(^1\text{D})$ with HCl, DCl, and Cl_2 . *J. Chem. Phys.* **1993**, *98* (10), 8330–8336.
9. Addison, M. C.; Donovan, R. K.; Garraway, J. Reactions of $\text{O}(2^1\text{D}_2)$ and $\text{O}(2^3\text{P}_j)$ with Halogenomethanes. *Faraday Discuss. Chem. Soc.* **1979**, *67*, 286–296.
10. Teixeira, O. B. M.; Marques, J. M. C.; Varandas, A. J. C. Dynamics Study of ClO + O_2 Collisions and Their Role in the Chemistry of Stratospheric Ozone. *Phys. Chem. Chem. Phys.* **2004**, *6* (9), 2179–2184.
11. Takahashi, K.; Hayashi, S.; Matsumi, Y. Quantum Yields of $\text{O}(^1\text{D})$ Formation in the Photolysis of Ozone between 230 and 308 Nm. **2002**, *107* (1).

12. “Phaseout of Class I Ozone-Depleting Substances” <https://www.epa.gov/ods-phaseout/phaseout-class-i-ozone-depleting-substances> (accessed September 15, 2019)
13. Environmental Protection Agency. Ozone-Depleting Substances. <https://www.epa.gov/ozone-layer-protection/ozone-depleting-substances> (accessed May 1, 2020)
14. B. J. Drouin, H. M. Pickett, Ozone line list catalogue number 48004, JPL online, <https://spec.jpl.nasa.gov/ftp/pub/catalog/catdir.html> (2005).
15. B. J. Drouin, Nitrous oxide line list catalogue number 44004, JPL online, <https://spec.jpl.nasa.gov/ftp/pub/catalog/catdir.html> (2014).
16. E. A. Cohen, Chlorine monoxide line list catalogue number 51002, JPL online, <https://spec.jpl.nasa.gov/ftp/pub/catalog/catdir.html> (1991).
17. Varberg, T. D.; Stroh, F.; Evenson, K. M. Far-Infrared Rotational and Fine-Structure Transition Frequencies and Molecular Constants of ^{14}NO and ^{15}NO in the $X^2\Pi$ ($v = 0$) State. *J. Mol. Spectrosc.* **1999**, *196* (1), 5–13.
18. B. J. Drouin, Nitric oxide line list catalogue number 30008, JPL online, <https://spec.jpl.nasa.gov/ftp/pub/catalog/catdir.html> (2010).
19. Hancock, G.; Haverd, V. Time Resolved FTIR Emission Measurements of the Internal Energies of NO Formed in the $\text{O}(^1\text{D}) + \text{N}_2\text{O}$ Reaction, and Energy Transfer Processes to N_2O . *Phys. Chem. Chem. Phys.* **2003**, *5* (11), 2369–2375.
20. Fernanders, Mariam S. *Crossed molecular beam study of $X + \text{O}_3$ ($X = \text{Br}$ and I) and $\text{O}(^1\text{D}) + X$ ($X = \text{Br}_2$, I_2 , CHCl_3 , N_2O) reactions via millimeter and sub-millimeter wavelength spectroscopy*. Greensboro, NC: University of North Carolina at Greensboro, 2014. Internet resource.
21. Cameo Chemicals. Chemical Datasheet. <https://cameochemicals.noaa.gov/chemical/5102> (accessed May 1, 2020)
22. Takahashi, K.; Hayashi, S.; Matsumi, Y. Quantum Yields of $\text{O}(^1\text{D})$ Formation in the Photolysis of Ozone between 230 and 308 Nm. *J. Geophys. Res.* **2002**, *107*.
23. Layne, B. H.; Duffy, L. M.; Carolina, N.; Bechtel, H. A.; Steeves, A. H.; Field, R. W. Beam Action Spectroscopy via Inelastic Scattering. *J. Phys. Chem. A* **2007**, *111*, 7398–7403.

24. The Ohio State University Department of Biochemistry and Chemistry Chemical Hygiene Plan. <https://chemistry.osu.edu/safety/chem/hygiene> (accessed March 14, 2019)
25. Takahashi, K.; Taniguchi, N.; Matsumi, Y.; Kawasaki, M. Translational Energy and Angular Distributions of O(¹D) and O(³P) fragments in the UV Photodissociation of Ozone. *Chem. Phys.* **1998**, *231*, 171–182.
26. Espinosa-garcía, J.; García-bernaldez, J. C. Vibrational versus Translational Energies in the H + CCl₄ Reaction: A Quasi-Classical Trajectory Study. *Chem. Phys. Lett.* **2011**, *502*, 48–52.
27. Polanyi, J. C. Some Concepts in Reaction Dynamics. *Acc. Chem. Res.* **1972**, *5* (5), 161–168.
28. Espinosa-garcia, J.; Rangel, C.; Monge-palacios, M.; Corchado, J. C. Kinetics and Dynamics Study of the H + CCl₄ → HCl (v', j') + CCl₃ Reaction. *Theor. Chem. Acc.* **2010**, *128* (July 2014), 743–755.
29. Zanchet, A.; Garci, E.; Aoiz, F. J.; Menéndez, M.; Jambrina, P. G. Λ - Doublet Propensities for Reactions on Competing A' and A'' Potential Energy Surfaces: O(³P) + N₂ and O(³P) + HCl. *J. Phys. Chem. A* **2018**, *122*, 2739–2750.
30. Jambrina, P. G.; Zanchet, A.; Aldegunde, J.; Brouard, M.; Aoiz, F. J. Product Lambda-Doublet Ratios as an Imprint of Chemical Reaction Mechanism. *Nat. Commun.* **2016**, *7*, 1–8.

APPENDIX A

CHLORINE MONOXIDE DATA

Table 3. Summary Table of Chlorine Monoxide Data in Appendix A

| Product | Rotational state transition $J' \leftarrow J''$ | Nuclear spin coupled with the rotational state $F' \leftarrow F''$ | Vibrational State transition $v' \leftarrow v''$ | Page / Figure |
|---------|--|---|---|---------------|
| ClO | 4.5 \leftarrow 3.5 | 3 \leftarrow 3 | 0 \leftarrow 0 | 57 / 27 |
| | 4.5 \leftarrow 3.5 | 4 \leftarrow 4 | 0 \leftarrow 0 | 56 / 25 |
| | 4.5 \leftarrow 3.5 | 5 \leftarrow 5 | 0 \leftarrow 0 | 56 / 24 |
| | 4.5 \leftarrow 3.5 | 6 \leftarrow 5 | 0 \leftarrow 0 | 57 / 26 |
| | 5.5 \leftarrow 4.5 | 7 \leftarrow 6 | 0 \leftarrow 0 | 57 / 28 |
| | 6.5 \leftarrow 5.5 | 8 \leftarrow 7 | 0 \leftarrow 0 | 58 / 29 |
| | 7.5 \leftarrow 6.5 | 9 \leftarrow 8 | 0 \leftarrow 0 | 58 / 30 |
| | 5.5 \leftarrow 4.5 | 7 \leftarrow 6 | 3 \leftarrow 3 | 58 / 31 |

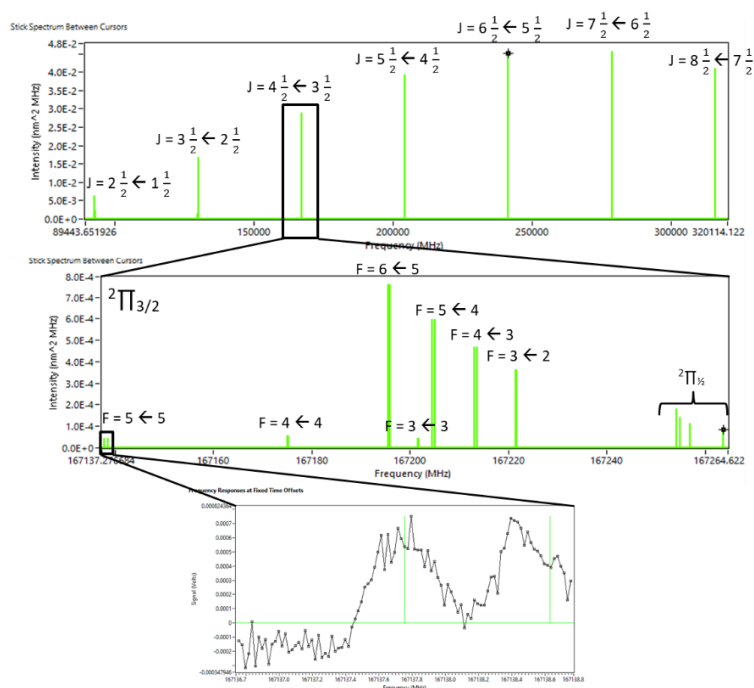


Figure 23. The Top Picture Shows the Frequencies for ClO That are Accessible Within Our Frequency Sources with the Middle Picture Showing One Rotational State Shown in Hyperfine Detail. The Bottom Picture Shows the Indicated Chlorine Monoxide Product Signal and Both Lambda Doublet Transitions.

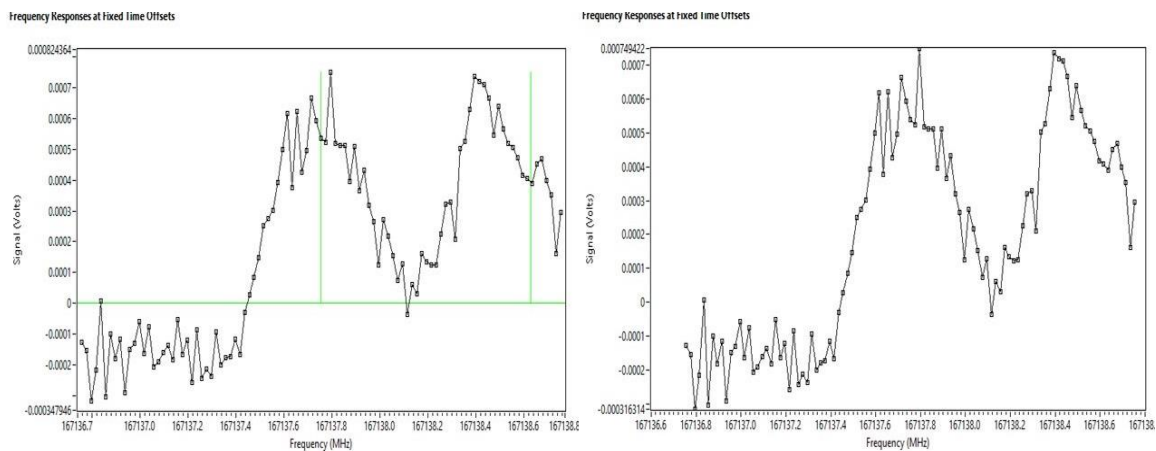


Figure 24. Absorption Signal for ClO With a Center Frequency of 167137.754900 MHz, Transitions Were $N = 4 \leftarrow 3$, $v = 0 \leftarrow 0$, $J = 4.5 \leftarrow 3.5$, $F = 5 \leftarrow 5$. The Left Peak Shows the Transition $\Lambda = 1 \leftarrow -1$, the Right Peak Being $\Lambda = -1 \leftarrow 1$.

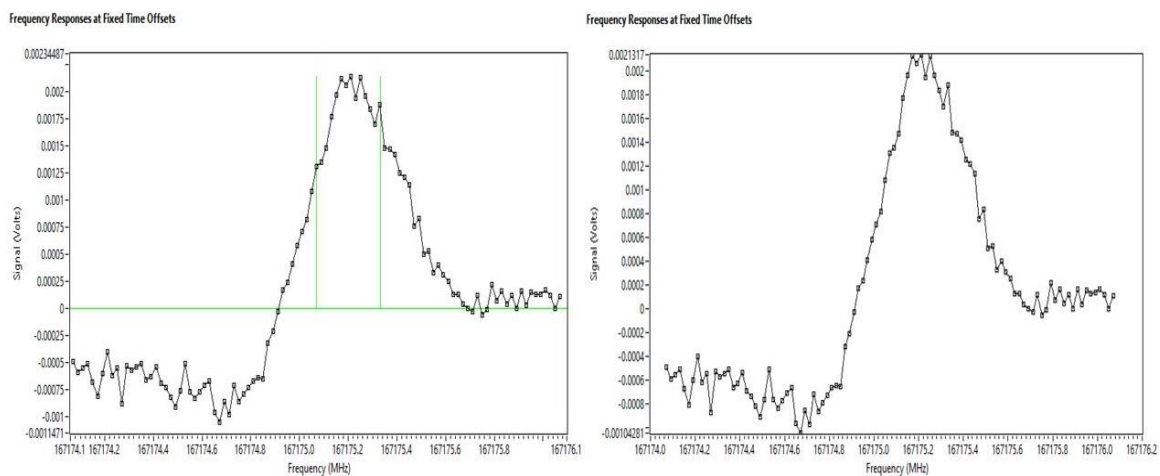


Figure 25. Absorption Signal for ClO With a Center Frequency of 167175.070600 MHz, Transitions Were $N = 4 \leftarrow 3$, $\Lambda = 1 \leftarrow -1$, $v = 0 \leftarrow 0$, $J = 4.5 \leftarrow 3.5$, $F = 4 \leftarrow 4$.

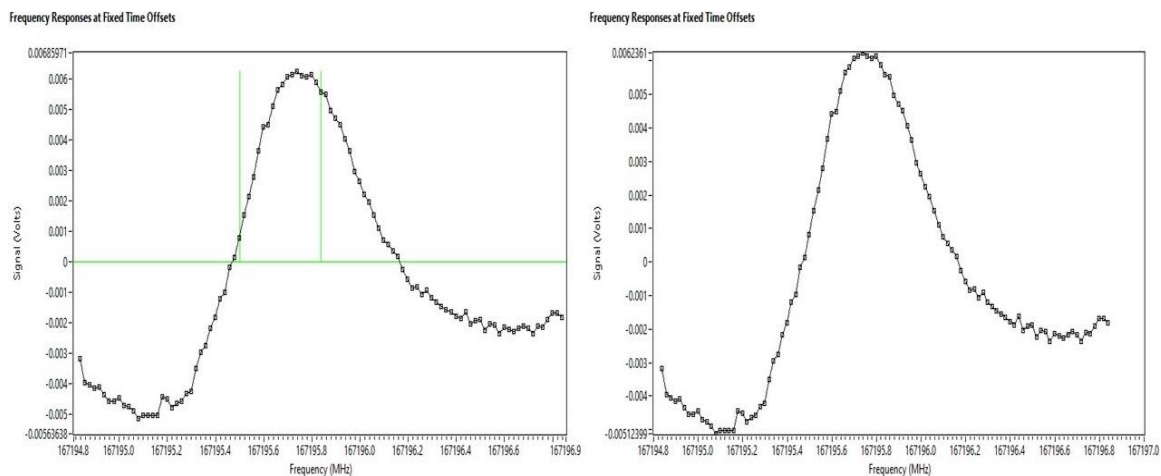


Figure 26. Absorption Signal for C1O With a Center Frequency of 167195.838000 MHz, Transitions Were $N = 4 \leftarrow 3$, $\Lambda = -1 \leftarrow 1$, $\nu = 0 \leftarrow 0$, $J = 4.5 \leftarrow 3.5$, $F = 6 \leftarrow 5$.

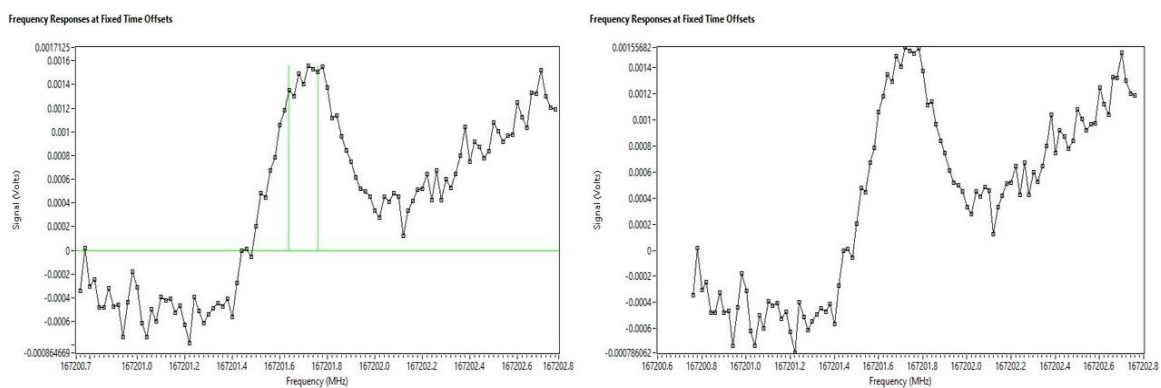


Figure 27. Absorption Signal for C1O With a Center Frequency of 167201.760800 MHz, Transitions Were $N = 4 \leftarrow 3$, $\Lambda = 1 \leftarrow -1$, $\nu = 0 \leftarrow 0$, $J = 4.5 \leftarrow 3.5$, $F = 3 \leftarrow 3$.

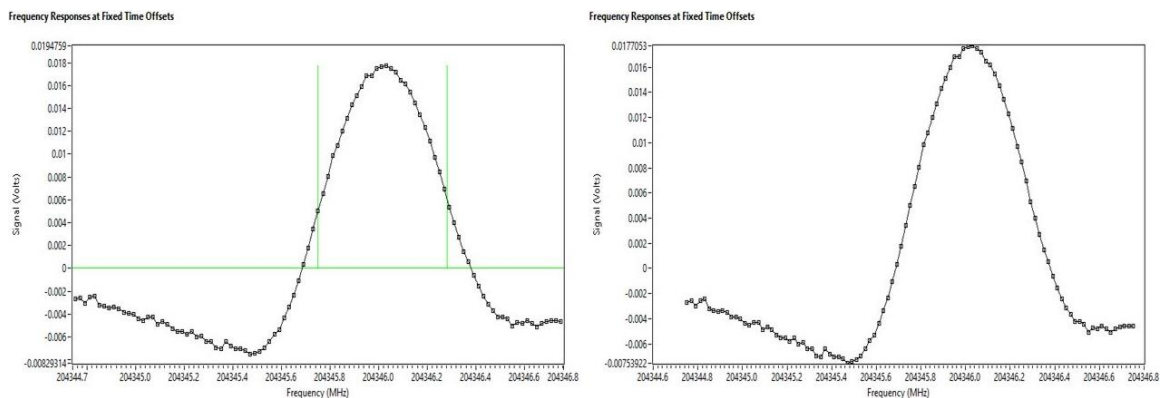


Figure 28. Absorption Signal for CIO With a Center Frequency of 204345.751100 MHz, Transitions Were $N = 5 \leftarrow 4$, $\Lambda = -1 \leftarrow 1$, $\nu = 0 \leftarrow 0$, $J = 5.5 \leftarrow 4.5$, $F = 7 \leftarrow 6$.

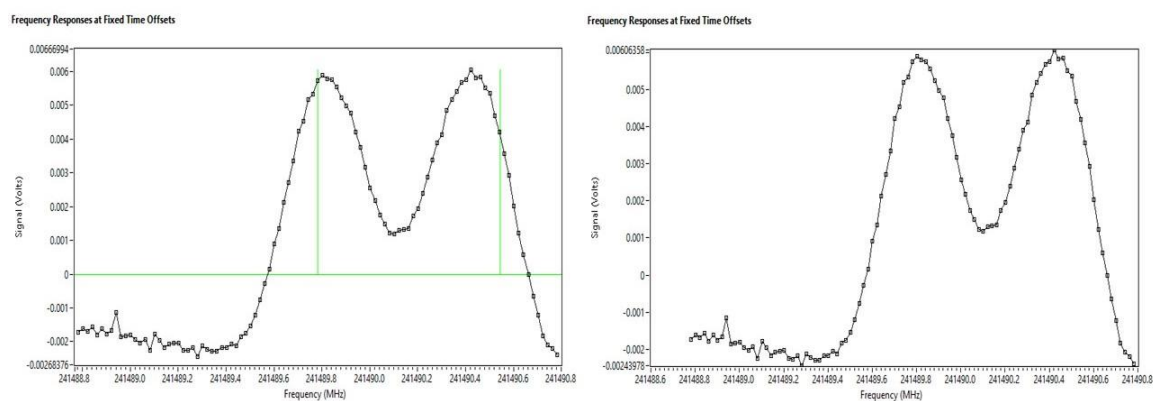


Figure 29. Absorption Signal for CIO With a Center Frequency of 241489.781700 MHz, Transitions Were $N = 6 \leftarrow 5$, $\nu = 0 \leftarrow 0$, $J = 6.5 \leftarrow 5.5$, $F = 8 \leftarrow 7$. The Left Peak Shows the Transition $\Lambda = 1 \leftarrow -1$, the Right Peak Being $\Lambda = -1 \leftarrow 1$.

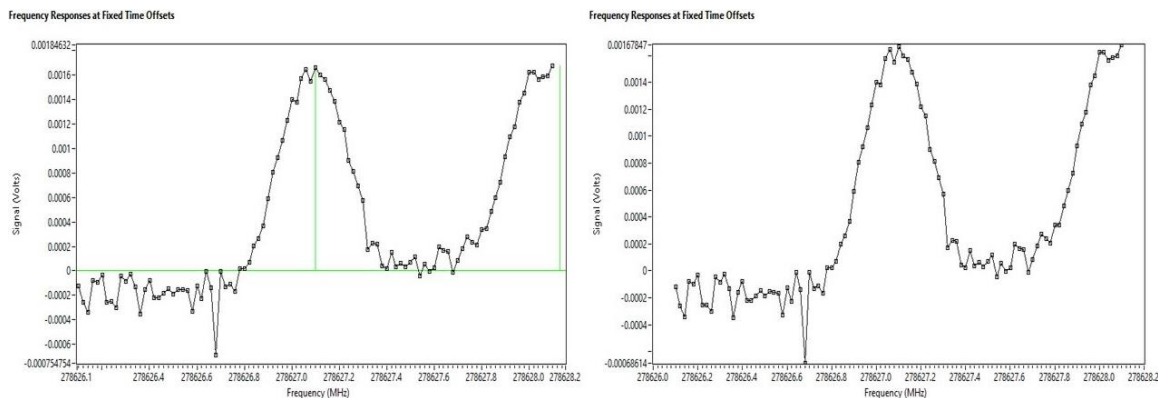


Figure 30. Absorption Signal for CIO With a Center Frequency of 278627.100200 MHz, Transitions Were $N = 7 \leftarrow 6$, $N = 0 \leftarrow 0$, $J = 7.5 \leftarrow 6.5$, $F = 9 \leftarrow 8$. The Left Peak Shows the Transition $\Lambda = -1 \leftarrow 1$, the Right Peak Being $\Lambda = 1 \leftarrow -1$.

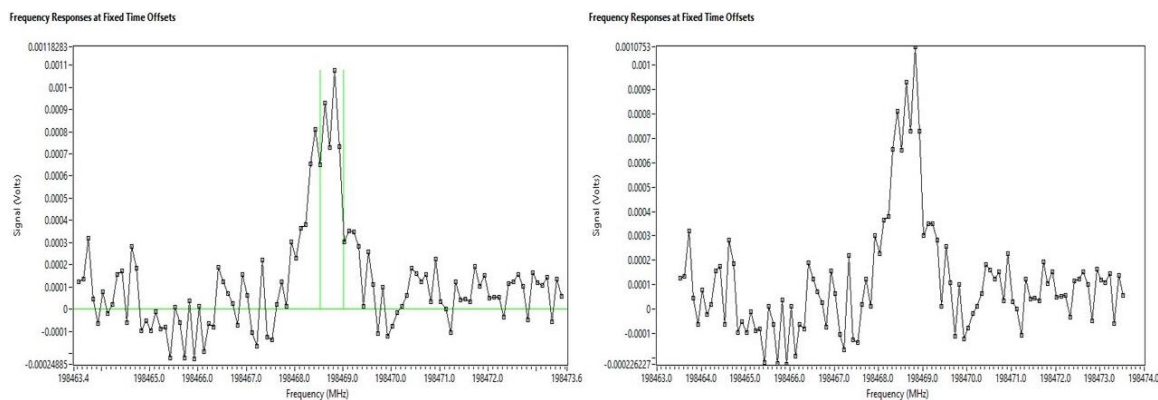


Figure 31. 2-D of Figure 20, Absorption Signal for CIO With a Center Frequency of 198468.525600 MHz, Transitions Were $N = 5 \leftarrow 4$, $\Lambda = -1 \leftarrow 1$, $v = 3 \leftarrow 3$, $J = 5.5 \leftarrow 4.5$, $F = 7 \leftarrow 6$.

APPENDIX B

NITRIC OXIDE DATA

Table 4. Summary Table of Nitric Oxide Data in Appendix B

| Product | Rotational state transition $J' \leftarrow J''$ | Nuclear spin coupled with the rotational state $F' \leftarrow F''$ | Orbital Angular momentum transition | Page / Figure |
|---------|--|---|-------------------------------------|---------------|
| NO | $1.5 \leftarrow 0.5$ | $0.5 \leftarrow 0.5$ | $-1 \leftarrow -1$ | 61 / 34 |
| | $1.5 \leftarrow 0.5$ | $0.5 \leftarrow 0.5$ | $1 \leftarrow -1$ | 62 / 36 |
| | $1.5 \leftarrow 0.5$ | $2.5 \leftarrow 1.5$ | $1 \leftarrow -1$ | 62 / 35 |
| | $1.5 \leftarrow 0.5$ | $2.5 \leftarrow 1.5$ | $-1 \leftarrow 1$ | 61 / 33 |
| | $2.5 \leftarrow 1.5$ | $1.5 \leftarrow 0.5$ | $1 \leftarrow -1$ | 64 / 40 |
| | $2.5 \leftarrow 1.5$ | $1.5 \leftarrow 1.5$ | $1 \leftarrow -1$ | 63 / 38 |
| | $2.5 \leftarrow 1.5$ | $2.5 \leftarrow 1.5$ | $1 \leftarrow -1$ | 65 / 41 |
| | $2.5 \leftarrow 1.5$ | $2.5 \leftarrow 2.5$ | $1 \leftarrow -1$ | 63 / 37 |

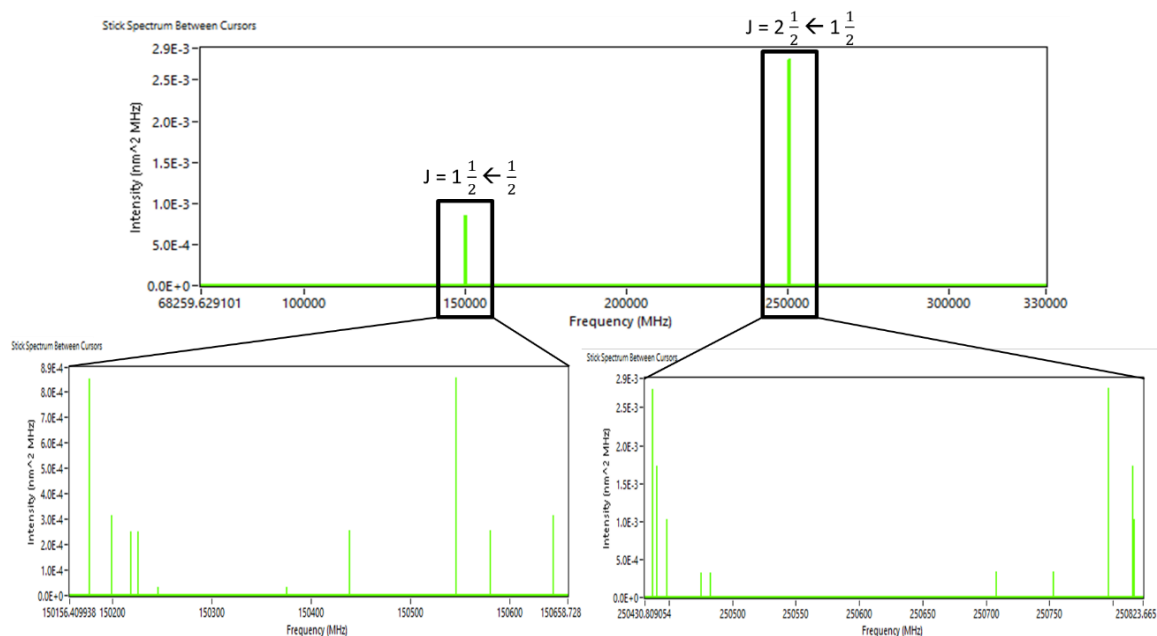


Figure 32. Frequencies for NO That are Accessible Within our Frequency Domain with One Rotational State Show in Detail to Show Multiple Line Frequencies and Their Transitions. The Bottom Frequencies Were Not Labeled Due to Their Not Being Any Uniformity to Them.

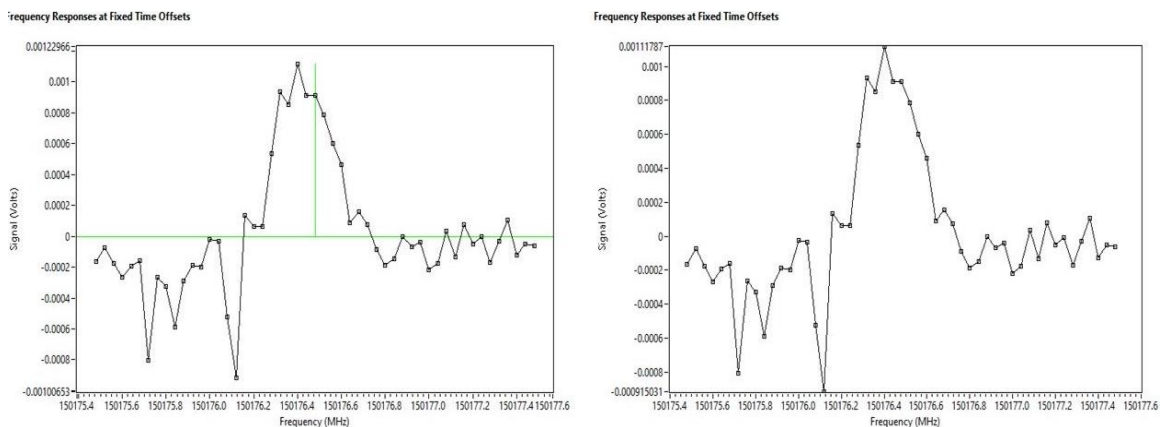


Figure 33. Absorption Signal for NO With a Center Frequency of 150176.480000 MHz, Transitions Were $N = 2 \leftarrow 1$, $A = -1 \leftarrow 1$, $v = 0 \leftarrow 0$, $J = 1.5 \leftarrow 0.5$, $F = 2.5 \leftarrow 1.5$.

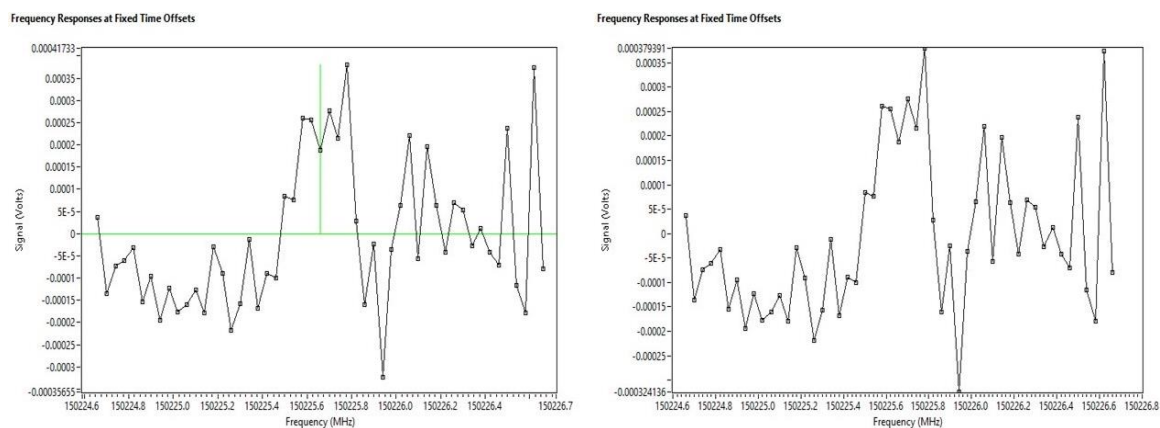


Figure 34. Absorption Signal for NO With a Center Frequency of 150225.660000 MHz, Transitions Were $N = 2 \leftarrow 1$, $A = -1 \leftarrow 1$, $v = 0 \leftarrow 0$, $J = 1.5 \leftarrow 0.5$, $F = 0.5 \leftarrow 0.5$.

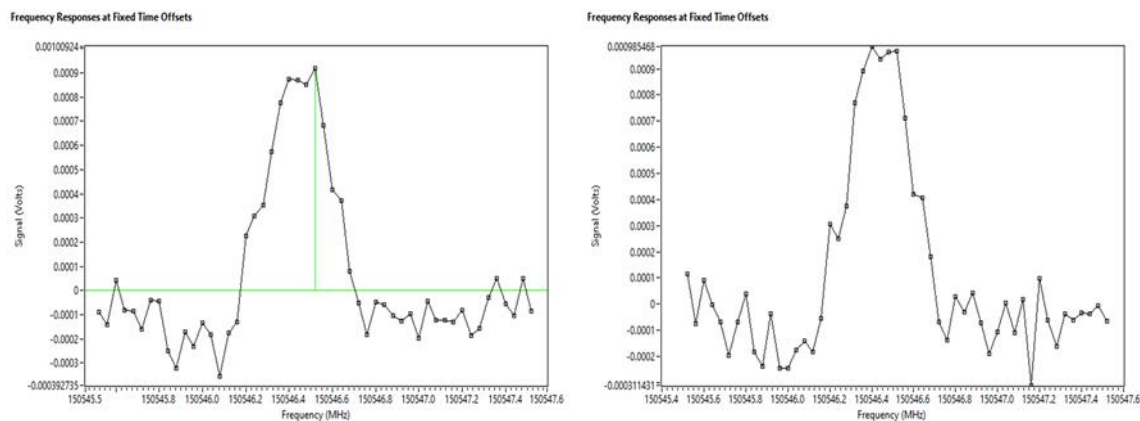


Figure 35. Absorption Signal for NO With a Center Frequency of 150546.520000MHz, Transitions Were $N = 2 \leftarrow 1$, $\Lambda = 1 \leftarrow -1$, $\nu = 0 \leftarrow 0$, $J = 1.5 \leftarrow 0.5$, $F = 2.5 \leftarrow 1.5$.

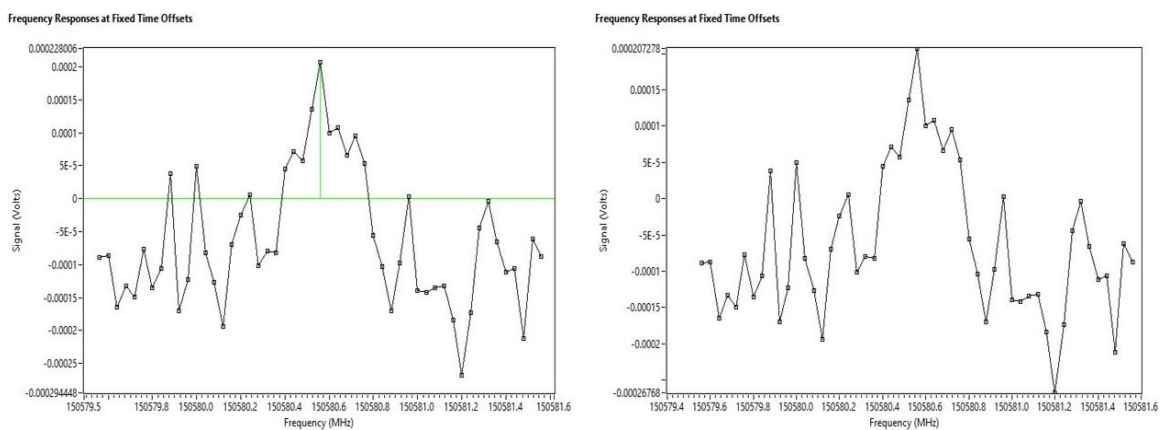


Figure 36. Absorption Signal for NO With a Center Frequency of 150580.560000MHz, Transitions Were $N = 2 \leftarrow 1$, $\Lambda = 1 \leftarrow -1$, $\nu = 0 \leftarrow 0$, $J = 1.5 \leftarrow 0.5$, $F = 0.5 \leftarrow 0.5$.

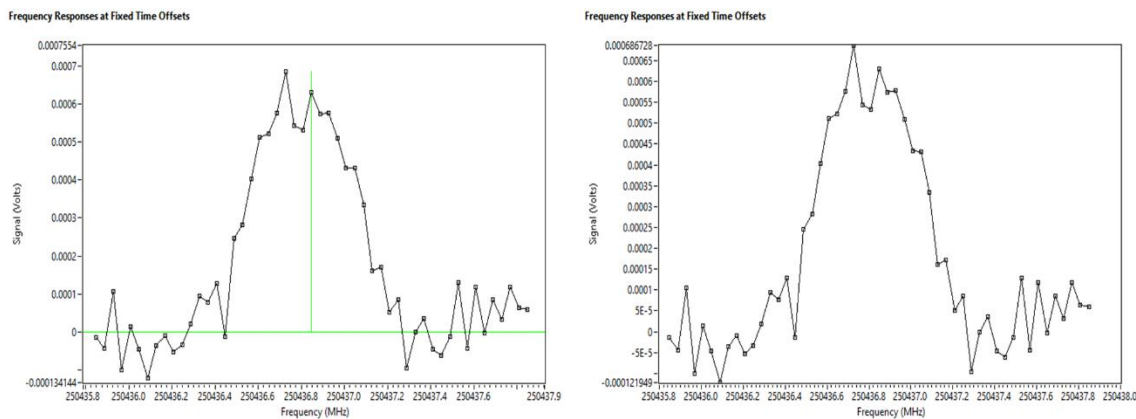


Figure 37. Absorption Signal for NO With a Center Frequency of 250436.8480 MHz, Transitions Were $N = 3 \leftarrow 2$, $\Lambda = 1 \leftarrow -1$, $\nu = 0 \leftarrow 0$, $J = 2.5 \leftarrow 1.5$, $F = 3.5 \leftarrow 2.5$.

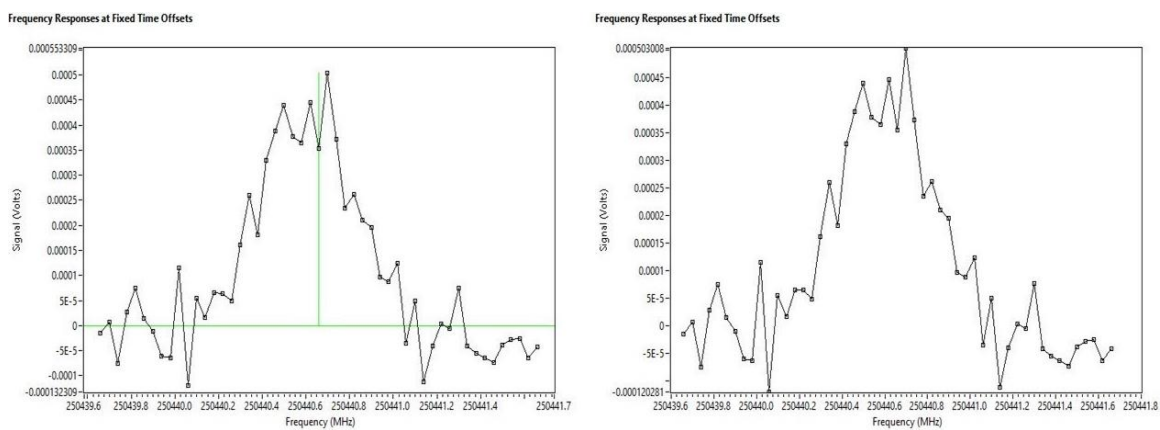


Figure 38. Absorption Signal for NO With a Center Frequency of 250440.6590 MHz, Transitions Were $N = 3 \leftarrow 2$, $\Lambda = 1 \leftarrow -1$, $\nu = 0 \leftarrow 0$, $J = 2.5 \leftarrow 1.5$, $F = 2.5 \leftarrow 1.5$.

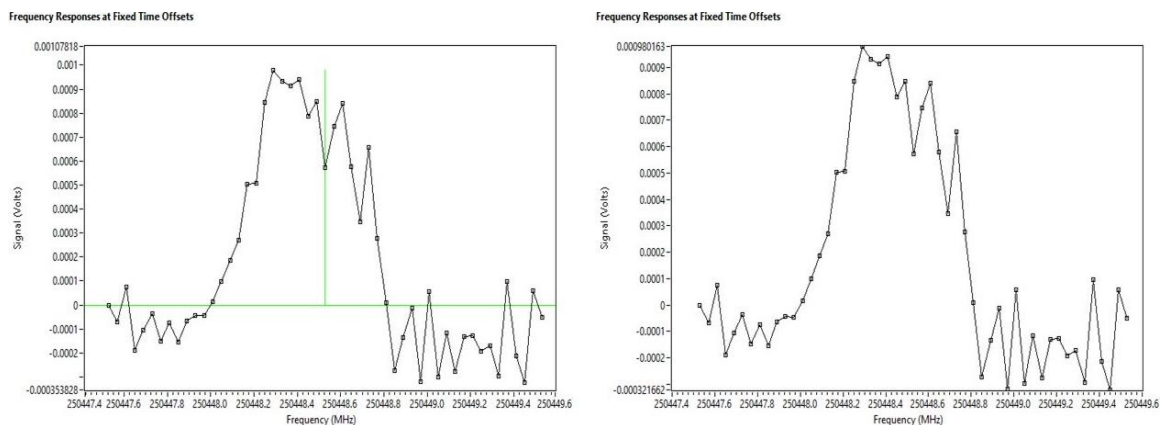


Figure 39. Absorption Signal for NO With a Center Frequency of 250448.53000 MHz, Transitions Were $N = 3 \leftarrow 2$, $\Lambda = 1 \leftarrow -1$, $v = 0 \leftarrow 0$, $J = 2.5 \leftarrow 1.5$, $F = 1.5 \leftarrow 0.5$.

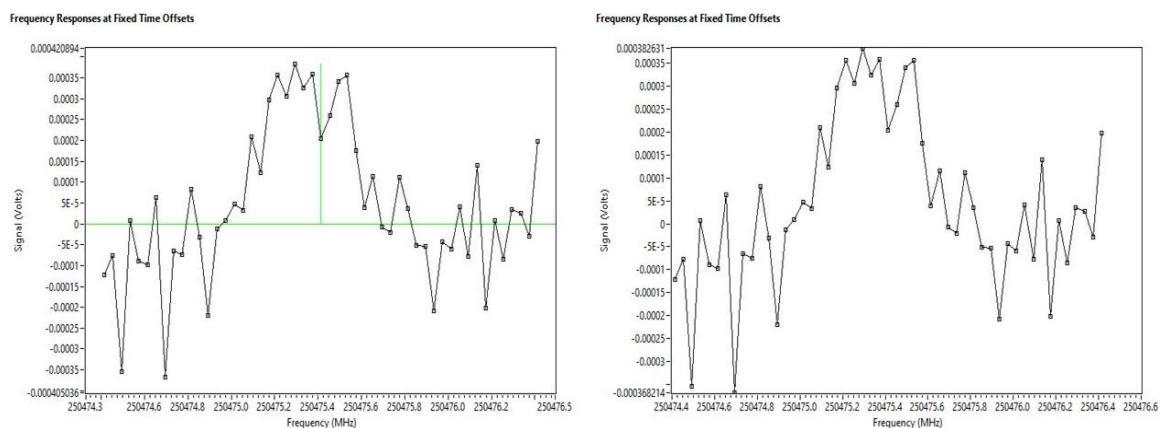


Figure 40. Absorption Signal for NO With a Center Frequency of 250475.41400 MHz, Transitions Were $N = 3 \leftarrow 2$, $\Lambda = 1 \leftarrow -1$, $v = 0 \leftarrow 0$, $J = 2.5 \leftarrow 1.5$, $F = 1.5 \leftarrow 1.5$.

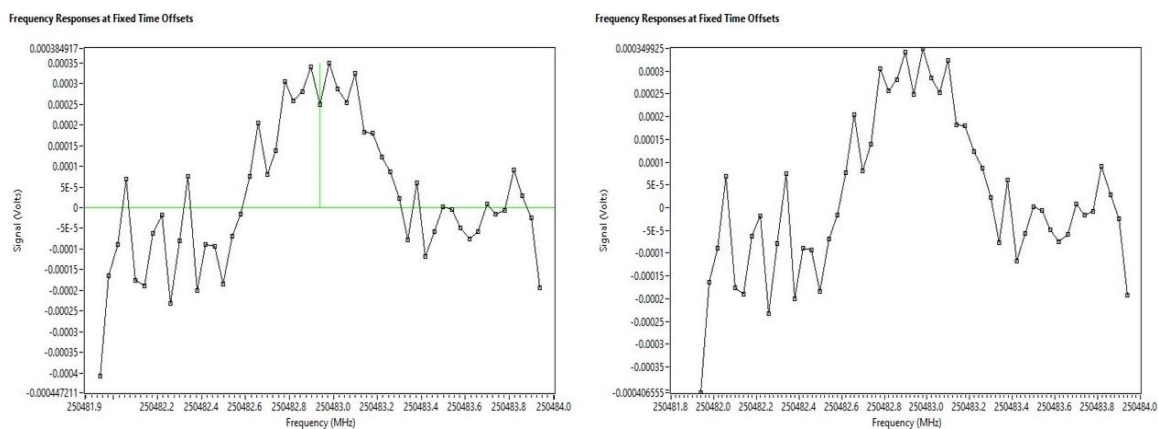


Figure 41. Absorption Signal for NO With a Center Frequency of 250482.939000 MHz, Transitions Were $N = 3 \leftarrow 2$, $A = 1 \leftarrow -1$, $v = 0 \leftarrow 0$, $J = 2.5 \leftarrow 1.5$, $F = 2.5 \leftarrow 2.5$.

APPENDIX C

OTHER DATA

Frequency Responses at Fixed Time Offsets

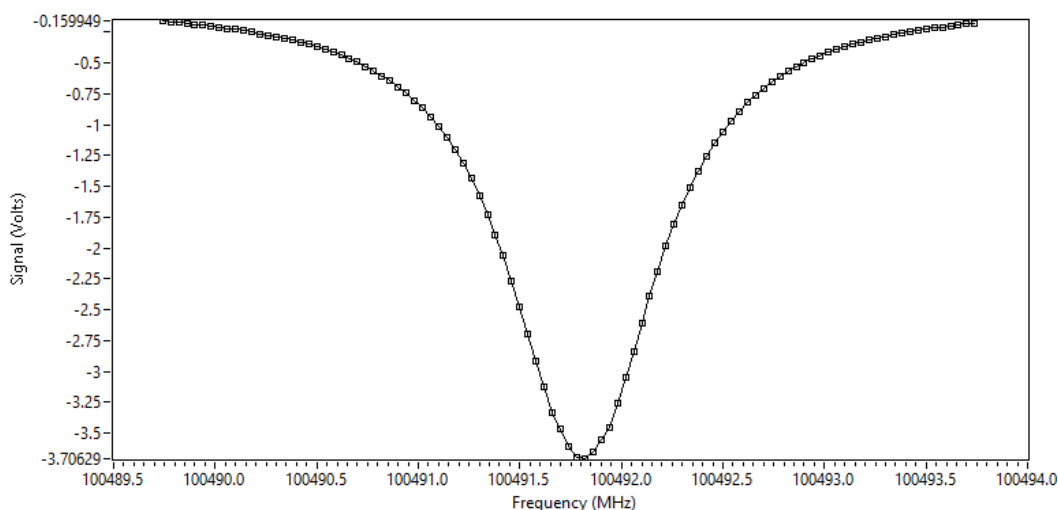


Figure 42. Scan of the Fabry-Pérot Cavity Resonance. A Negative Signal Here Indicated More Power Making It Through to the Detector. Using Eqn. 10, the Resonance Yields a Cavity $Q = n / Dn$ on the Order of 115,000.

Frequency Responses at Fixed Time Offsets

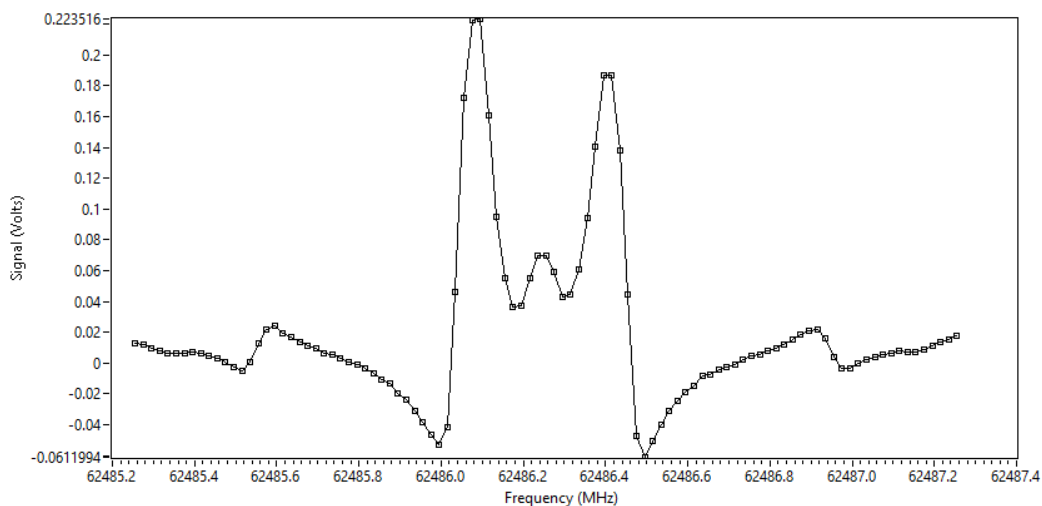


Figure 43. Absorption Signal for Magnetic Dipole Allowed Transition of O_2 With a Center Frequency of 62486.259400 MHz, Transitions Were $N = 3 \leftarrow 3$, $J = 0 \leftarrow 0$, $F_1 = 0 \leftarrow 0$, $F_2 = 3 \leftarrow 2$.

Frequency Responses at Fixed Time Offsets

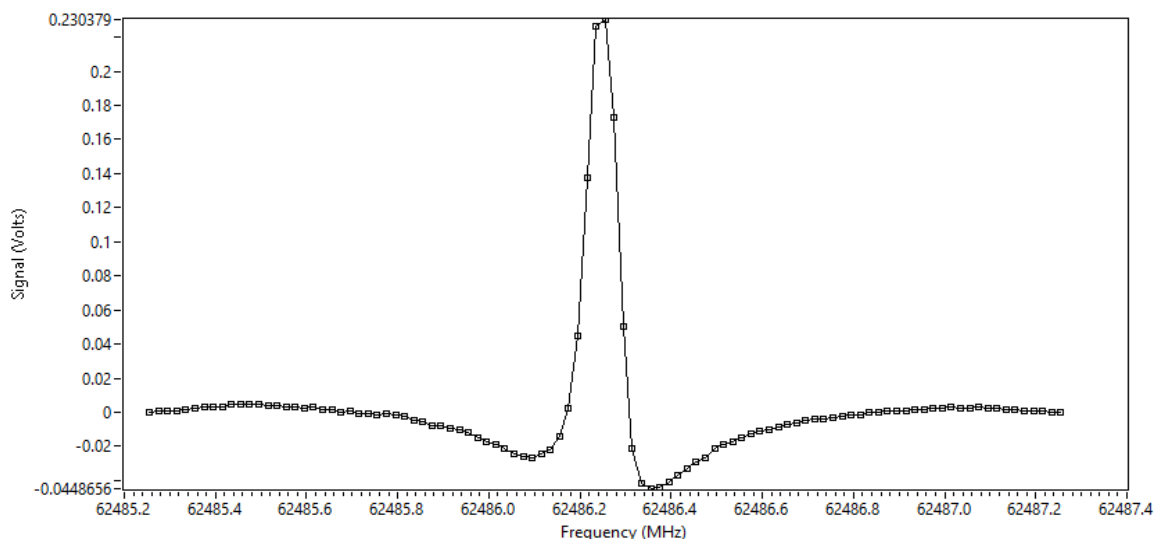


Figure 44. Absorption Signal for O_2 With a Center Frequency of 62486.259400 MHz, Transitions Were $N = 3 \leftarrow 3$, $J = 0 \leftarrow 0$, $F_1 = 0 \leftarrow 0$, $F_2 = 3 \leftarrow 2$. A Magnet Was Placed Downrange and Above the Molecular Beam and Was Used to See if it Could Manipulate the Signal Since the Signal is Absorption of the Magnetic Dipole Moment Instead of an Electric Dipole Moment.

Frequency Responses at Fixed Time Offsets

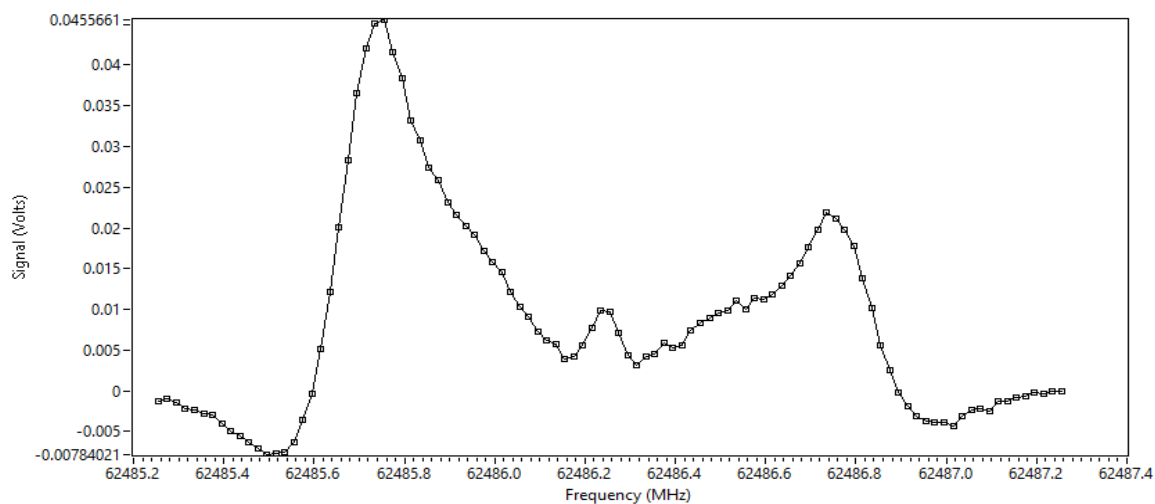


Figure 45. Absorption Signal for O_2 With a Center Frequency of 62486.259400 MHz, Transitions Were $N = 3 \leftarrow 3$, $J = 0 \leftarrow 0$, $F_1 = 0 \leftarrow 0$, $F_2 = 3 \leftarrow 2$. A Magnet was Placed Left and Above of the Molecular Beam and Was Used to See if it Could Manipulate the Signal Since the Signal is Absorption of the Magnetic Dipole Moment Instead of an Electric Dipole Moment.

Frequency Responses at Fixed Time Offsets

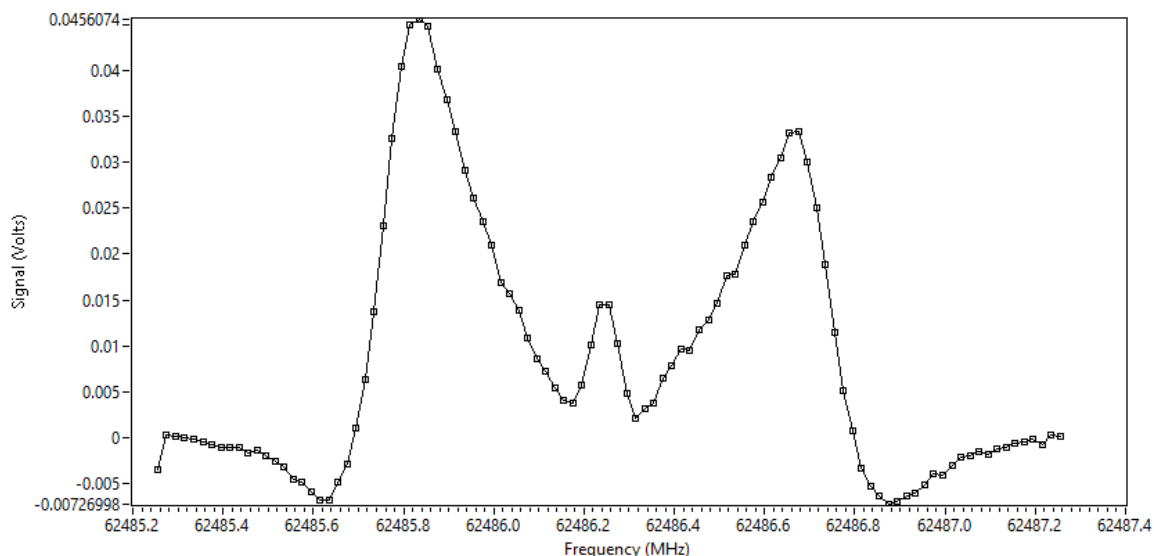


Figure 46. Absorption Signal for O_2 With a Center Frequency of 62486.259400 MHz, Transitions Were $N = 3 \leftarrow 3$, $J = 0 \leftarrow 0$, $F_1 = 0 \leftarrow 0$, $F_2 = 3 \leftarrow 2$. A Magnet Was Placed Right and Above of the Molecular Beam and Was Used to See if it Could Manipulate the Signal Since the Signal is Absorption of the Magnetic Dipole Moment Instead of an Electric Dipole Moment.

Frequency Responses at Fixed Time Offsets

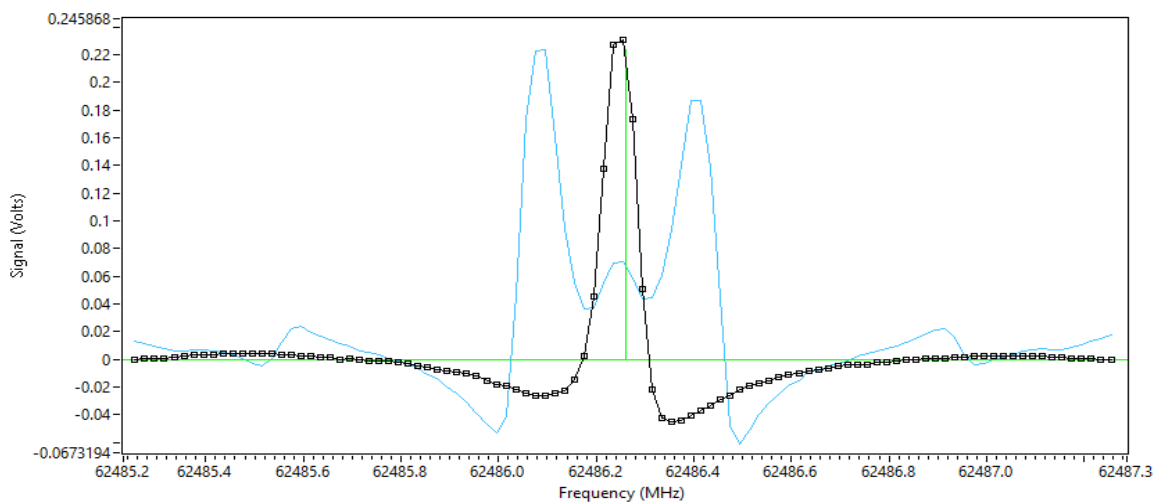


Figure 47. Absorption Signal for O_2 With a Center Frequency of 62486.259400 MHz, Transitions Were $N = 3 \leftarrow 3$, $J = 0 \leftarrow 0$, $F_1 = 0 \leftarrow 0$, $F_2 = 3 \leftarrow 2$. A Direct Comparison Between the O_2 Absorption Peak with No Magnet and With the Magnet Down Range and Above the Molecular Beam.

Frequency Responses at Fixed Time Offsets

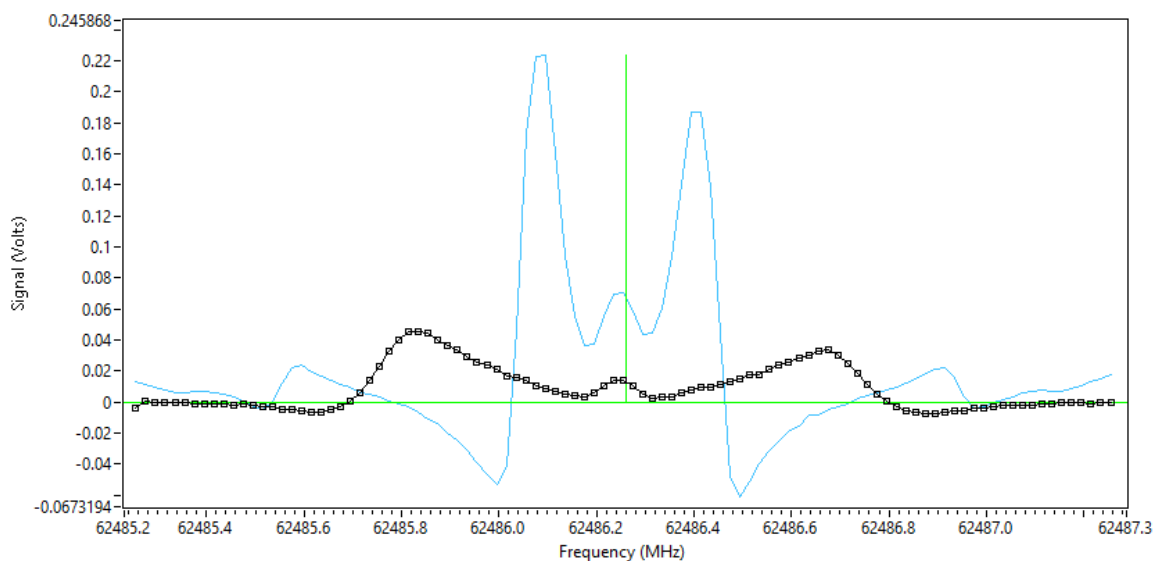


Figure 48. Absorption Signal for O_2 With a Center Frequency of 62486.259400 MHz, Transitions Were $N = 3 \leftarrow 3$, $J = 0 \leftarrow 0$, $F_1 = 0 \leftarrow 0$, $F_2 = 3 \leftarrow 2$. A Direct Comparison Between the O_2 Absorption Peak with No Magnet and With the Magnet to the Left and Above the Molecular Beam. Similar Results Were Seen with the Magnet to the Right and Above the Molecular Beam as Well.